

**Bio-Mechanical Applications of Electrospun Polycaprolactone (PCL)  
Nanofibers**

**By**

**Harsha Jamadagni**

Master of Science in Engineering Physics-Mechanical Engineering

University of Central Oklahoma

Edmond, Oklahoma

2017

Master Thesis

Submitted to the Faculty of

the Graduate collage of the University of Central Oklahoma

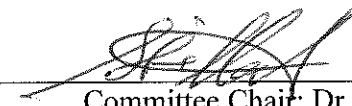
in partial fulfillment of the requirements for Degree of

Master of Science

December, 2017


**Bio-Mechanical Applications of Electrospun Polycaprolactone (PCL)  
Nanofibers**

Thesis Approved:



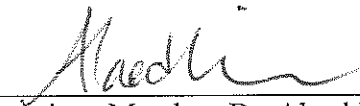
---

Committee Chair: Dr. Morshed Khandaker



---

Committee Member: Dr. Mohammad Hossan



---

Committee Member: Dr. Alaeddin Abuabed

## ACKNOWLEDGMENTS

I would like to express my deepest sense of appreciation to my advisor, Dr. Morshed Khandaker, for the continuous support of my master study and research, for his patience, motivation, enthusiasm, and immense knowledge. His guidance helped me in all the time of research and writing of this thesis. I could not have imagined having a better advisor and mentor for my master study.

I am thankful to Dr. Mohammad Hossan and Dr. Alaeddin Abu-Abed for their encouragement, insightful comment, and support during my research.

I acknowledge my gratitude to the National Institute of General Medical Sciences of the National Institutes of Health under award number, 5P20GM103447. I am also indebted to the Department of Engineering and Physics, the College of Mathematics and Science, and Graduate collage at University of Central Oklahoma.

I would like to thanks my professors during the graduate studies and my research mates for cooperation and guidance.

Finally, I take this opportunity to express the profound gratitude from my deep heart to my beloved parents for their love and continuous support.

## Abstract

Due to its low cost, biocompatibility and slow bioresorption, poly-ε-caprolactone (PCL) continues to be a suitable material for select biomedical engineering applications. In this study, we have concentrated on improving the efficiency of the titanium, bone cement and polymeric membrane by modify each of the materials surface characteristics.

The first part of the study evaluated both experimentally and numerically the effect of surface modification on a titanium implant to the load transfer characteristics from implant to bone for examining stress shielding parameters. This study measured the effect of micron grooves on titanium to the mechanical stability of titanium using a rabbit model. This study also developed a finite element model based on the *in vivo* test model to examine the stress shielding parameters. The results showed that the mean values of fracture strength were significantly higher for grooved titanium samples compared to the samples without any groove and unequal load sharing due to micro-grooving causes an increase in stiffness of the adjacent bone to the implant.

The second part of the study is based on the hypothesis that the PCL nanofiber membrane (NFM) on PMMA will increase biocompatibility without influencing its mechanical properties. This study prepared PMMA samples without and with the PCL NFM coating, which were named the control and NFM coated samples. This study determined the effects on the surface topography of each group of PMMA. This study found that the NFM coating on PMMA significantly improved the surface roughness and cytocompatibility properties of PMMA ( $p < 0.05$ ). Therefore, the developed PCL NFM coating technique on PMMA has potential in clinical applications.

The third part of the study evaluated the immobilization of metal oxide (MO) nanoparticles (NPs) for a gas sensor research. The goal of this project was to immobilize three different metal oxide (MO) nanoparticles (NPs) (MgO, TiO<sub>2</sub>, ZnO) with PCL NFM to create each MO-PCL NFM. The scanning electron microscopy analysis of the fabricated membranes confirmed that MO NPs reached the collector along with the polymer solution during the electrospinning process.

## Table of Contents

1 INTRODUCTION .....	12
1.1 Electrospinning.....	12
1.2 Materials investigated in this study .....	13
1.2.1 Titanium.....	13
1.2.2 Bone Cement.....	13
1.2.3 Metal Oxide Nanoparticles (MO-NPs).....	13
1.2.4 PEGDA .....	14
1.3 Motivation and goals .....	14
1.4 Objectives .....	14
1.5 Organization of the thesis .....	15
2 EFFECT OF MICRO-GROOVING ON THE STRESS SHIELDING OF TITANIUM: EXPERIMENTAL AND NUMERICAL INVESTIGATIONS .....	16
2.1 Summary.....	16
2.2 Background and Significance.....	16
2.3 Materials and methods.....	17
2.3.1 Experimental model.....	17
2.3.2 Finite Element model.....	18
2.4 Results and discussion .....	22
2.4.1 Experimental analysis.....	22
2.4.2 Finite Element analysis.....	22
2.5 Conclusion .....	25
3 Use of Polycaprolactone Electrospun Nanofibers as a Coating for Poly(methyl methacrylate) Bone Cement.....	26
3.1 Summary.....	26
3.2 Background and Significance.....	26
3.3 Materials and Methods .....	28
3.3.1 Materials .....	28
3.3.2 Sample Preparation.....	28

3.5.2.1 Sample Design .....	28
3.5.2.2. Sample Fabrication Process .....	29
(a) Fiber Production .....	29
(b) Surface Characterization and Mechanical Test Samples .....	30
(c) Cytocompatibility Test Samples .....	31
3.4 Experiments and Analysis .....	32
3.4.1 Surface Topography.....	32
3.4.2 Cell Adhesion, Proliferation, Mineralization, and Protein Adsorption Tests on PMMA Samples.....	32
3.4.3 Mechanical Tests .....	34
3.4.4 Statistical Analysis.....	34
3.5 Results .....	35
3.5.1 Surface Topography.....	35
3.5.2 Cytocompatibility Properties .....	36
3.5.3 Mechanical Tests .....	40
3.6 Discussion.....	41
3.7 Conclusions .....	46
4 Immobilization and characterization of metal oxides in an electrospun nanofiber membrane for gas detection .....	47
4.1 Summary.....	47
4.2 Goals and Objectives.....	47
4.3 Background and Significance.....	48
4.4 Experimental Design and Methods.....	48
4.5 Results and Discussion.....	49
4.6 Future works.....	51
5. Evaluation of Polyethylene Glycol Diacrylate-polycaprolactone scaffolds for a tissue engineering application	
5.1 Summary.....	52
5.2 Background and Significance.....	52

5.3 Materials and methods.....	54
5.3.1 Materials .....	54
5.3.2 Sample preparation .....	54
5.5.2.1 Sample design .....	54
5.5.2.2 Sample fabrication process .....	54
5.3.3 Experiments .....	56
5.5.3.1. SEM and histological examination.....	56
5.5.3.2. Mechanical tests.....	57
5.5.3.3 Bioactivity.....	57
A. Absorption test.....	57
B. Cell Cultures .....	57
C. Cell Viability Assay .....	57
D. Microscopy and Staining .....	58
5.4 Results .....	59
5.4.1 Fabrication of an electrospin unit for the production of PEGDA scaffold.....	59
5.4.2 Surface characterization.....	60
5.4.3 Mechanical tests.....	61
5.4.4 Bioactivity.....	63
5.5 Discussion.....	66
5.6 Conclusions .....	68

## List of Figures

Figure 1-1 Schematic of electrospinning set up.....	12
Figure 2-1: Pull out tension test on titanium/bone sample .....	18
Figure 2-2: Boundary condition of the FEA model.....	20
Figure 2-3: Load-displacement graph for an implant-rabbit bone without and with grooves.....	22
Figure 2-4: MicroCT image of a titanium/bone sample. ....	23
Figure 2-5: Mesh structure of FEA model of a Ti/bone sample.....	23
Figure 2-6: (a) Stress distributions at the implant/bone interface and (b) Local stress distribution around first thread.....	24
Figure 2-7: Stress transfer parameters. ....	25
Figure 3-1: Schematic representation of the production methods for (a) single layer aligned PCL ENF production; (b) surface characterization/mechanical test samples; and (c) cytocompatibility test samples.....	29
Figure 3-2: (a) Fabrication of aligned PCL fibers for coating using the electrospinning process; (b) Collected fibers on a glass slide. ....	30
Figure 3-3: (a) Fabricated mold used for curing cement; (b) A cured PMMA cement in the mold; (c) A red dyed ENF coated cement sample on the chamber of the Hitachi TM 1000 scanning electron microscope; and (d) ASTM standard three-point bend PMMA cement specimen.....	31
Figure 3-4: (a) ENF discs which were pressed on the top of PMMA during the doughy phase of the cement; (b) Control and ENF coated PMMA samples in an acrylic mold which were used for cytocompatibility tests.....	32
Figure 3-5: Three-point bend fixture for determining the bending properties of the bone cement. ....	34
Figure 3-6: Scanning electron microscope images of the (a) control and (b) electrospun nanofiber (ENF) coated Poly(methyl methacrylate) (PMMA) specimen.....	35
Figure 3-7: A representative fluorescent stained image (100× total magnification, scale bar = 500 μm) from adhesion and proliferation assays showing adhered (blue color) and proliferated cells (green color) of the (a) control and (b) ENF coated PMMA samples.....	37
Figure 3-8: Mean cell adhesion density (± standard error) and the percentage of cell proliferation (± standard error) for the control and ENF coated PMMA groups after 48 h of cell culture. Data are presented with n = 14 for both samples. Note: * p < 0.05 (compared to control).....	38



Figure 3-9: A representative fluorescent stained image (100× total magnification, scale bar = 500 μm) from the mineralization assays showing the released mineral (green) from the cells of the (a) control and (b) ENF coated PMMA samples after 3 weeks of cell culture .....	39
Figure 3-10: A representative fluorescent stained image (100× total magnification, scale bar = 500 μm) from the protein adsorption assays showing osteoblast nuclei (blue) and released osteonectin (red) from the cells of the (a) control and (b) ENF coated PMMA samples after 3 weeks of cell culture. ....	39
Figure 3-11: Mean amount of mineralization (± standard error) and mean amount of osteonectin (± standard error) for the control and ENF coated PMMA groups. Note: * p < 0.05 (compared to control). ....	40
Figure 3-12: Typical stress vs. strain plots of the control and ENF coated PMMA specimens. The observed difference between the maximum stress and strain values in the figure is due to the difference of the dimensions and internal structures of the samples.....	41
Figure 4-1 Schematic image of the creation of MO-PCL NFM .....	49
Figure 4-2: SEM image showing the presence of MgO NPs in a PCL fiber: (a) MgO, (b) ZnO and TiO <sub>2</sub> NPs added PCL.....	51
Figure 5-1: Schematic representation of a PEGDA-PCL scaffold [65]. The process b-c-d can be repeated multiple times to create higher thickness scaffold. ....	56
Figure 5-2: (a) An integrated electrospun-UV photo polymerization-machine; (b) Twelve layers of aligned PCL ENF deposited on the acrylic mold; fabricated samples (c) PEGDA and (d) PEGDA-PCL.....	60
Figure 5-3: SEM images of top surface of (a) PEGDA and (b) PEGDA-PCL scaffolds. PCL-PEGDA samples shows higher amount of artifacts in compare to PEGDA. SEM images of paraffin embedded and sectioned scaffolds: (c) PEGDA and (d) PCL-PEGDA. Red arrows in Figure 4d shows the presence of PCL ENF in PEGDA. ....	61
Figure 5-4: Load vs. displacement plot of a PEGDA and PEGDA-PCL scaffold under static compression loading.....	62
Figure 5-5: Rheological tests were performed on the hydrogel using the Malvern CVO-100 rheometer at 5% strain rate at frequency 1 Hz. (a) shear stress vs. strain and (b) complex modulus with respect to time was found from the experiment. ....	63
Figure 5-6: DMEM absorption rate with respect time. Note: *p<0.05 (compared to PEGDA).....	64
Figure 5-7: GS5 cells attached to 12 layers of PCL nanofiber (Panel BF and CF) sandwiching the PEGDA scaffold. Panel BS and CS represent cells growing embedded in PEGDA. Panel AF and AS are control scaffold without cells. White	

arrows point to cells. All scaffolds were incubated for 7 and 14 days. Images were taken using Leica light microscope at 100X total magnification..... 65

Figure 5-8: H&E staining of PEGDA-PCL scaffolds with GS5 cells (Panel B) after 7 days. Black arrows in panel B point to cells. Panel A is control scaffold without any cells. Leica light microscope at 400X magnification..... 65

Figure 5-9: Increase in cell number on PEGDA-PCL scaffold with time. GS5 cell Viability after 7 and 14 days on PCL-PEGDA scaffolds using alamarBlue® assay. Our results clearly indicate that cells remain viable on our scaffolds. Values are mean  $\pm$  SD of triplicates..... 66

## List of Tables

Table 2-1: Material properties of each geometry.....	19
Table 3-1: Difference of roughness between control and electrospun nanofiber (ENF) coated Poly(methyl methacrylate) (PMMA) samples. Data are presented as mean $\pm$ standard error. Data are presented with n = 3 for both samples. Note: p < 0.05 is denoted by * and p < 0.01 by ** (compared to control).....	36
Table 3-2: Summary statistics for the cell viability tests with respect to the cell culture time by sample group. Data are presented as mean $\pm$ standard error. Data are presented with n = 28 for both samples. Note: p < 0.05 is denoted by * and p < 0.01 by ** (compared to control).....	38
Table 3-3: Summary statistics for the three-point bend test experimental data by sample group. Data are presented with n = 10 for both samples. Data are presented as mean $\pm$ standard error. Note: * p < 0.05 (compared to control).....	41
Table 5-1: Difference between mechanical properties between PEGDA and PEGDA-PCL scaffolds during compression. Both samples have same diameters (10 mm) and loaded up to 35 N to calculate the mechanical properties. Data presented n=3 for both samples. Data presented as a mean $\pm$ standard error. Note: *p<0.05 (compared to PEGDA).....	62
Table 5-2: Difference between viscoelastic properties between PEGDA and PCL-PEGDA scaffolds. Both samples have same diameters (9.56 mm). Data presented n=3 for both samples. Data presented as mean $\pm$ standard error. Note: *p<0.05 (compared to control).....	63

# Chapter 1

## INTRODUCTION

### 1.1 Electrospinning

Electrospinning is a simple method and popular technique for the fabrication of macro to nanofibers. Due to its simplicity, the applications of electrospun nanofibers can be seen in a broad range of fields including biomedical applications such as drug delivery, tissue engineering, wound dressing and cosmetics, functional materials and devices such as composite reinforcement, filters, protective clothing and smart textiles, and energy and electronics such as batteries/cells and capacitors, sensors and catalysts. (<https://www.ncbi.nlm.nih.gov/pubmed/19076051>)

The electro-spinning set up includes a high voltage supplier, pump injection, collector, small diameter tube, syringe, and needle. In the electro spinning process, a required polymer is dissolved in a suitable solvent to form a polymer solution which is then put in a syringe and fixed in a syringe pump. A high voltage source is used to create an electrical field. Positive pole connects to the needle of the syringe and the collector electrodes are grounded. Schematic of electrospinning set up is shown in Figure 1-1.

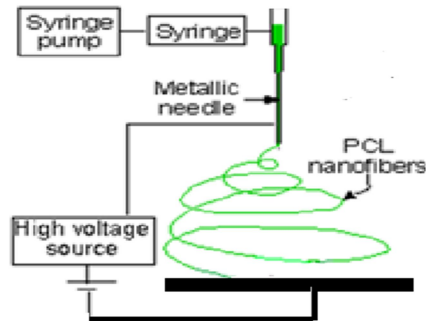


Figure 1-1 Schematic of electrospinning set up

## 1.2 Materials investigated in this study

### 1.2.1 Titanium

Titanium based alloy have been widely used in orthopedic and orthodontic surgeries as implants because of their strong mechanical, chemical (corrosion resistance), and biological properties and biocompatibility [1-3]. In this particular study, Ti-6AL-4V was used as it is the most widely used material for implants because of its better physical and mechanical properties compared to pure Ti.

Micron size grooves were created on the 2.2mm dia Ti rod using Full spectrum laser machine to analyze the effect of surface modification on a titanium implant to the load transfer characteristics from implant to bone for examining stress shielding parameters.

### 1.2.2 Bone Cement

Polymethylmethacrylate (PMMA) is being used widely in most orthopedic surgeries because of its strong mechanical bonding with implant. The bone cement used in this study was Cobalt (Biomet, Inc.) HV PMMA bone cement and Veterinary bone cement (Bio Medtrix, LLC). PMMA bone cements are provided as two-component materials, a powder (PMMA beads) and a liquid (MMA monomer) which polymerizes when mixed at 2:1 ratio. The goal of studying this material is to see if we can increase the osseointegration at the tissue-cement interface by improving the bioactivity of cement so that it will mimic the native tissue-tissue failure response under functional loading.

### 1.2.3 Metal Oxide Nanoparticles (MO-NPs)

Sensing material is commonly the key part of the gas sensor. Therefore, the development of sensors mainly focuses on exploring high-performance sensing materials. Metal oxide nanomaterials are widely used to fabricate efficient gas sensors for the detection of various hazardous and toxic gasses. For example, MgO is used for SO<sub>2</sub> gas sensors [4], TiO<sub>2</sub> NP is used for low-temperature CO<sub>2</sub> gas sensors [5], ZnO NP is used for

NO<sub>2</sub> gas sensors [6]. Electrospun PCL nanofibers having a high surface area-to-volume ratio can be used as a carrier for MO-NPs for gas sensing applications. The effect of the immobilization of each of the MOs with PCL and characterization is carried out in this study.

#### 1.2.4 PEGDA

Tissue engineering (TE) holds great promise for the cultivation of patient-specific tissues for restoring organ functions and/or curing various diseases [1-3]. Photosensitive hydrogels, such as Polyethylene Glycol Diacrylate (PEGDA) are an important class of biomaterials with many TE applications [7-9]. Photolithography is a commonly used process in micro-fabrication to produce the desired scaffold with specific shape and size using a mold [10]. The ability to control the porosity of photosensitive hydrogel such as Polyethylene Glycol Diacrylate (PEGDA) to elicit altered cell behaviors, including cell adhesion, has raised heightened interest in the scaffold materials for various biomedical applications such as orthopedic repair and regeneration [11] and liver tissue engineering [12]. This material study focuses on the physical, mechanical and biological capabilities of PEDGA-PCL scaffold and evaluate the capabilities for tissue engineering applications.

#### 1.3 Motivation and goals

The motivation of this thesis was to evaluate the effect of PCL nanofibers on different materials: Titanium implants, Bone cement, Metal oxide nanoparticles and PEGDA. The goals were to measure the effect of PCL nanofibers on Ti implants, Bone cement and PEGDA by conducting in-vivo and in-vitro tests. In addition to this, the goal also included the determination of the structure and morphology of the Metal Oxide – PCL – Nanofiber mesh (MO-PCL-NFM) by scanning electron microscopy (SEM).

#### 1.4 Objectives

The objectives of this thesis are: 1) Effect of micro-grooving on the stress shielding of titanium: Experimental and numerical investigations. 2) Use of

polycaprolactone electrospun nanofibers as a coating for poly(methyl methacrylate) bone cement. 3) Immobilization and characterization of metal oxides in an electrospun nanofiber membrane for gas detection 4) Evaluation of Polyethylene Glycol Diacrylate-polycaprolactone scaffolds for a tissue engineering application

### 1.5 Organization of the thesis

This thesis contains six chapters. Chapter 1 is the introduction of the thesis. In Chapter 2 measured the effect of micron grooves on titanium to the mechanical stability of titanium using a rabbit model. This study also developed a finite element model based on the in vivo test model to examine the stress shielding parameters. Chapter 3 was to evaluate the in vitro effects of the PCL ENF coating on the surface topography and cytocompatibility (osteoblast cell adhesion, proliferation, mineralization, and protein adsorption) properties of PMMA bone cement. This study also determined the effect of the PCL ENF coating on the mechanical properties of the PMMA bone cement under three-point bend loading. In chapter 4, the structure and morphology of the MO-PCL-NFM was determined. The goal Chapter 5 is to study physical, mechanical and biological capabilities of PEDGA-PCL scaffold and to evaluate the capabilities for tissue engineering applications.

## CHAPTER 2

### EFFECT OF MICRO-GROOVING ON THE STRESS SHIELDING OF TITANIUM: EXPERIMENTAL AND NUMERICAL INVESTIGATIONS

#### 2.1 Summary

Micron sizes grooves can control the cell settlement on the implant surface or be used to direct tissue generation at the implant/bone interface. The effect of shape, size and the type of material of the microgrooves on the mechanical stimulus transfer from the implant to bone at physiological loading is not known yet. Therefore, this study evaluated both experimentally and numerically the effect of surface modification on a titanium implant to the load transfer characteristics from implant to bone for examining stress shielding parameters. This study measured the effect of micron grooves on titanium to the mechanical stability of titanium using a rabbit model. This study also developed a finite element model based on the in vivo test model to examine the stress shielding parameters. The results showed that the mean values of fracture strength were significantly higher for grooved titanium samples ( $1.32 \pm 0.45$  MPa,  $n = 3$ ) compared to control samples (without any groove) ( $0.22 \pm 0.16$  MPa,  $n=6$ ) ( $P < 0.05$ ). The load-displacement graph from the pull out tension tests were used to measure the frictional coefficient between Ti and bone from the FEA model. It was found from the FEA model that the average co-efficient of friction between titanium and bone was 0.48. Maximum equivalent stress along the interface of microgrooves on titanium were higher from groove area in compare to non-groove area because the change of the geometry along the groove. The microgrooves in the model has significant effect on the stress transfer parameter between implant and adjoining bone. The unequal load sharing due to micro-grooving causes an increase in stiffness of the adjacent bone to the implant.

#### 2.2 Background and Significance

Micron to nanometer size groove topography can be created on the implant surface using surface cutting and etching techniques [13-16]. We have shown that osteoblast cells are especially responsive to groove created by laser peening that induce higher amount of osteoblast cell adhesion and proliferation compared to titanium (Ti) samples without grooves [17]. Cells



align and migrate on the grooves [14, 18]. Such surface modifications can enhance mechanical stability of the implant by increasing the amount of implant contact area for bone growth.

Implant loosening due to stress shielding has been reported by several researchers [19]. Stress shielding of bone, which is the reduction in bone density (osteopenia) as a result of removal of stress from the bone by the implant is one of the reasons for implant loosening. Excessive bone resorption, in part due to stress shielding, is a recurrent problem leading to implant loosening[20]. Surface topography of implants are known to influence the rate of bone remodeling surrounding the implant [21, 22]. Research showed strong influences of groove topography on stress transfer from implant to bone for initiating the bone remodeling process [21, 22]. However, the effects of groove architecture (such as depth, shape, number of groove and distance between the grooves on the implant–bone interaction) are not known. Such knowledge is important for finding the suitable groove topography for implants that will provide the optimum biomechanical compatibilities of the implants. Since the mechanical stimuli transfers from implants to bone and affects the rate of bone remodeling and stress shielding in the bone, it is necessary to quantify and compare how these design parameters reflect upon mechanical stimuli distributions within bone. Computational means such as finite element analysis (FEA) is the most feasible approach for evaluating mechanical stimuli distributions in implant-bone constructs [23, 24]. In this study, we aimed to quantify the mechanical stimuli to the bone adjacent to Ti due to the presence of microgrooves on titanium by an *in vivo* animal model and finite element modeling of the Ti/bone sample to find the stress shielding parameters due to grooving.

## 2.3 Materials and methods

### 2.3.1 Experimental model

Using a rabbit model of implant integration, we have tested the effect of submicron grooves of Ti on the mechanical stability of Ti. A 2 mm diameter × 12 mm length medical grade Ti rod (6Al-4V ELI) was used as implant for *in vivo* studies. The detail of animal study protocol will appear in a journal. In short, Buehler Isomet diamond saw cutter and a custom made motorized holder were used to cut total twenty parallel circumferential grooves at a distance 0.5 mm from an edge of Ti rod. Two groups of samples were used: Ti without grooves (control) and

with microgrooves. Each group of samples was implanted in the femoral condyle of 4 week old New Zealand White Rabbits (NWR) at The University of Oklahoma Health Sciences Center (OUHSC) according to the approved OUHSC IACUC procedure. The operation sites of the rabbits were shaved and sterilized, and followed by decortication. Bilateral implantations were performed under anaesthetization at the epiphyso–metaphyseal junction on both legs. A 6 mm deep hole was made at the junction using a 1.96 mm diameter drill tool; Ti samples were then hand-pressed into the prepared holes. X-ray images of the implantation sites were conducted immediately after surgery to measure the depth of implant inside the bone. The animal was euthanized after 8 weeks of surgery. Soft tissues were carefully cleaned and bone was dissected by the saw machine. A custom made fixture was used to permit coaxial alignment of the implant in the direction of pull-out force (**Error! Reference source not found.**). The implant was carefully fastened to the top gripper in the mechanical tester and slowly lowered to embed the sample in a low-viscosity acrylic bone cement. Tension tests were conducted on each sample at room temperature with a steady speed of 0.3 mm/min[25]. The maximum pull-out force from load-displacement curve was measured and mechanical stability (quantified by fracture strength) was calculated by dividing the force at the point of failure by the surface area of Ti in contact with bone.

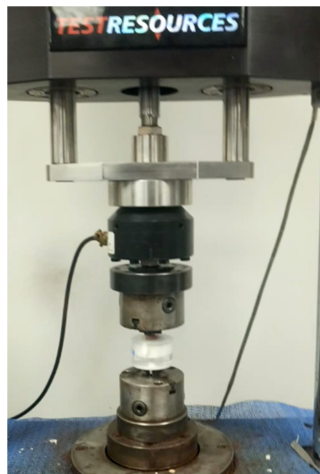


Figure 2-1: Pull out tension test on titanium/bone sample

### 2.3.2 Finite Element model

Calculation of frictional coefficient between titanium and bone:

Ti/bone 3D model was generated in SolidWorks 2013 from microCT scan image of the Ti/bone sample. CAD model was imported to model and analyze finite elements model into ANSYS Workbench Static Structural. To carry out Finite elements analyses, material properties are defined. Linear elastic and homogenous isotropic material models were used to describe bone. Titanium alloy (6Al-4V ELI) was purchased from Supra alloy Inc. Material property was found the data sheet as provided by Supra alloy. Material properties of each geometry was shown Table 2-1.

	Materials		
	Titanium	Cortical	Trabecular
Young's Modulus (GPa)	116	3.3	71
Poisson's ratio	0.32	0.35	0.35

Table 2-1: Material properties of each geometry

After assigned material properties for each geometry, suitable mesh structure and size were determined for geometry. The 8-node hexhedral (ANSYS solid 186) were assigned for each geometry. Ti-bone cement samples were meshed with element body size of 0.2 mm and 0.4 mm element size. All of surfaces on implant-bone interface were meshed with a 0.10-mm face element size by using local face element size, since there were many sharp discontinuities that could induce an unrealistically high stress concentration. While the element size is determined, attention has been paid to ensure that the results are independent of the mesh structure. Using the aspect ratio and element quality checks, all elements were within acceptable limits, thus increase the accuracy of the results. Deformation of Ti rod at Z axis was applied in the FEA model, which is the experimental displacement of Ti rod break from the cement in the direction normal to the Ti rod top surface (**Error! Reference source not found.-2**). Von-Mises stress, also referred as equivalent tensile stress, is used to check whether the design will withstand a given load condition. Only Z directional displacement was allowed for the micro-grooved Ti implant. Bounded contact was defined between bone cement and support. The interface between the Ti

and bone was also set as contact, with frictional coefficients for the surface contacts of the rough implant surface with the cement bone for prediction of frictional coefficient.

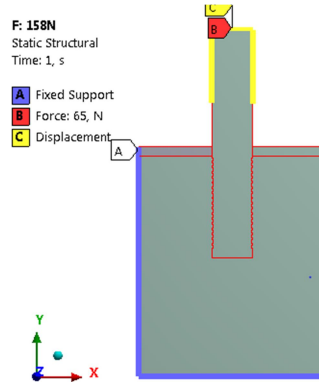


Figure 2-2: Boundary condition of the FEA model.

Calculation of stress shielding parameters:

This study took into consideration two different kinds of mechanical stimulus (stress and strain energy density) which are required for initiation bone remodeling. In order to investigate the effect of grooves on mechanical stimulus, Haase *et al.* [22] approach for the prediction of stress shielding around an implant was used. In short, effective stress distribution, represented as  $\sigma_{vm}$  (von Mises equivalent), which is expressed by tension stress,  $\sigma_{ts}$  and compression stress,  $\sigma_{cs}$  using Eq (1).

$$\sigma_{vm} = (\sigma_{ts}^2 + \sigma_{cs}^2 - \sigma_{ts} \sigma_{cs})^{0,5} \quad (1)$$

Stress transfer parameters (STP) (Eqs. 2, 3, and 4) provide a quantitative dimensionless evaluation of the load transfer between implant and adjoining bone with implant for understanding bone remodeling and osteosynthesis post-implantation.

$$STP_{\alpha} = \frac{\sigma_{b1}}{\sigma_{t1}} \quad (2)$$

$$STP_{\beta} = \sum_{i=j=2}^{i=j=N} \frac{\sigma_{bi}}{\sigma_{tj}} \quad (3)$$

$$STP_{Toplam} = STP_{\alpha} + STP_{\beta} \quad (4)$$

In the above equations,  $\sigma_{bi}$  and  $\sigma_{tj}$  are average stress values within bone and in near bounded screw, respectively. Subscripts  $\alpha$  and  $\beta$  represent stress and strain energy density transfer on first thread and all other thread, respectively.  $N$  represents the number of threads.

In case of assuming bone materials as a linear elastic isotropic, strain energy density transfer parameters (SEDTP) (Eqs 5,6, and 7) was used that also characterizes the load sharing between implant and bone.

$$SEDTP_{\alpha} = \frac{\sigma_{b1} \varepsilon_{b1}}{\sigma_{t1} \varepsilon_{t1}} \quad (5)$$

$$SEDTP_{\beta} = \sum_{i=j=2}^{i=j=N} \frac{\sigma_{bi} \varepsilon_{bi}}{\sigma_{tj} \varepsilon_{tj}} \quad (6)$$

$$SEDTP_{total} = SEDTP_{\alpha} + SEDTP_{\beta} \quad (7)$$

In the above equations,  $\varepsilon_{bi}$  and  $\varepsilon_{tj}$  strain within bone and in adjacent screw. All of these values were taken from along screw thread.

STP and SEDTP quantitatively dimensionless evaluations of load sharing were separated for first thread and all other thread due to first thread carries majority of load, which may cause high stress concentration in compare to the other threads.

In the present study, the CAD model was developed using SolidWorks, it was then automatically imported to ANSYS Workbench (FEA Software) for the parametric studies. Implant groove dimension were parametrized by controlling the associated parameters by Excel VBA programming.

## 2.4 Results and discussion

### 2.4.1 Experimental analysis

**Error! Reference source not found.** shows the load vs displacement plots of a Ti/bone samples without and with grooves. The mean values of fracture strength, which was calculated from the load vs. displacement data were significantly higher for grooved Ti samples ( $1.32 \pm 0.45$  MPa,  $n = 3$ ) compared to without-groove (control) samples ( $0.22 \pm 0.16$  MPa,  $n=6$ ) ( $P < 0.05$ ). The results concluded that grooves improved the mechanical stability of the Ti. There is high variance of fracture strength for the grooved samples, which is due to the variation of groove depth.

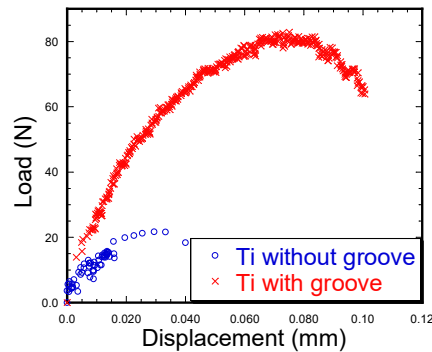


Figure 2-3: Load-displacement graph for an implant-rabbit bone without and with grooves.

The result showed the mechanical stability of Ti samples with microgrooves was almost 6 times higher compared to Ti samples without microgrooves. The study also showed that the breakage of non-grooved Ti samples occurred at the implant-bone interfaces, whereas microgrooved Ti sample breakage occurred at bone in the vicinity of implant.

### 2.4.2 Finite Element analysis

#### Frictional coefficient between titanium and bone:

In order to determine frictional coefficient of Ti microgroove implant, a pull out tension test result from an *in vivo* test sample was used. The frictional coefficients of Ti-rabbit bone were calculated based on an experiment load-displacement graph from the sample. The failure load of

158,14N has corresponding displacement 0.10973mm according to the Ti microgroove implant experiment results. A FE model was developed based on the microCT image from the Ti/bone sample (**Error! Reference source not found.**).

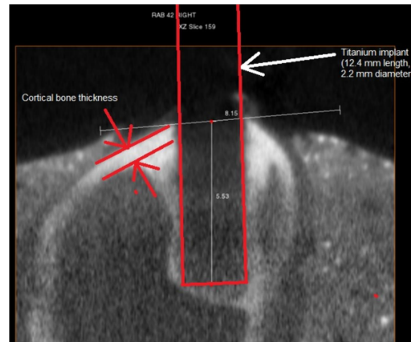


Figure 2-4: MicroCT image of a titanium/bone sample.

The FEA results shows that frictional coefficient value of 0.5 best represent the experimental load vs. displacement values with %7.4 of error for Ti/bone samples having grooves.

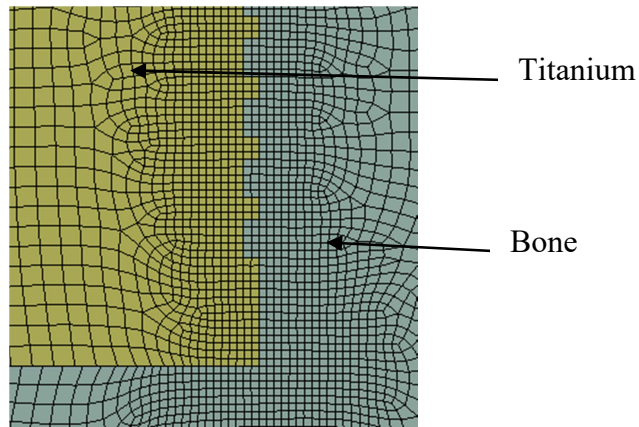


Figure 2-5: Mesh structure of FEA model of a Ti/bone sample.

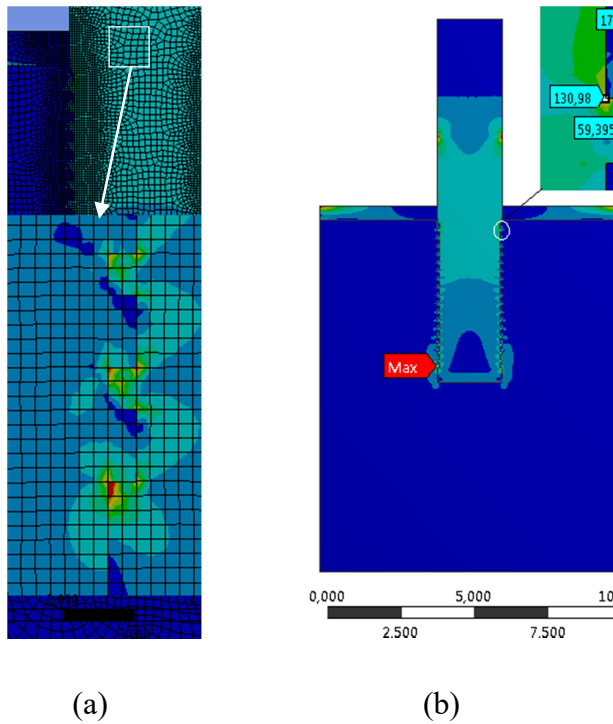


Figure 2-6: (a) Stress distributions at the implant/bone interface and (b) Local stress distribution around first thread.

Stress shielding parameters:

According to our FEA results, stress distributions on the cortical bone is shown in **Error! Reference source not found.a**. A significant increase in stress value is observed along the length of the Ti/bone interface. The stress values around the implant can be explained by the contact between the two different material surfaces. Higher equivalent Von-mises stress was observed along the edges of the microgrooves. However, high stress concentration was observed on first thread and last three threads from the edge inside the bone. Maximum stress value was obtained on the apex of last thread (**Error! Reference source not found.b**). According to our FEA results, there is significant stress difference between Ti implant which is stiffer material and trabecular bone which is softer material. This situation is explained by effect of stress shielding in the literature[24].

Load sharing has been characterized by using two of mechanical stimulus. However, effect of micro-grooving on stress shielding was evaluated by using previously defined parameters such as STP (Stress transfer parameters) and SEDTP. Results are presented in **Error! Reference source**



**not found..** In the figure,  $\alpha$  represents stress transfer from first thread to surrounding bone.  $\beta$  represents the stress transfer to the surrounding bone on the all other threads portion. Microgrooves provide more uniform stress distribution on the surrounding bones and implants (**Error! Reference source not found.b**). This can be explained by the fact that the micro-groove increases the contact area at the interface and affects the results.

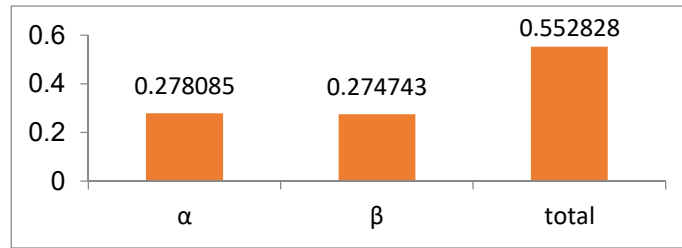


Figure 2-7: Stress transfer parameters.

## 2.5 Conclusion

The in vivo animal study results concluded that grooves improved the mechanical stability of the Ti. There is high variance of fracture strength for the grooved samples, which is due to the variation of groove depth. A parametric model was developed to compare bone stresses due to presence of microgrooves on Ti using finite element analysis. A set of stress-transfer parameters was used to quantify the transfer of mechanical stimuli to bone due to topographical change of microgrooves on Ti implants. The model can be used to determine the optimum topography of microgrooves on Ti which will give better mechanical stimuli from Ti to bone for minimizing stress shielding effects.

**Acknowledgement:** I would like to acknowledge Lokesh Dhanasekaran at the University of Central Oklahoma and Hasan Karaman at Uludag University for the above collaborative work.

## CHAPTER 3

### USE OF POLYCAPROLACTONE ELECTROSPUN NANOFIBERS AS A COATING FOR POLY(METHYL METHACRYLATE) BONE CEMENT

#### 3.1 Summary

Poly(methyl methacrylate) (PMMA) bone cement has limited biocompatibility. Polycaprolactone (PCL) electrospun nanofiber (ENF) has many applications in the biomedical field due to its excellent biocompatibility and degradability. The effect of coating PCL ENF on the surface topography, biocompatibility, and mechanical strength of PMMA bone cement is not currently known. This study is based on the hypothesis that the PCL ENF coating on PMMA will increase PMMA roughness leading to increased biocompatibility without influencing its mechanical properties. This study prepared PMMA samples without and with the PCL ENF coating, which were named the control and ENF coated samples. This study determined the effects on the surface topography and cytocompatibility (osteoblast cell adhesion, proliferation, mineralization, and protein adsorption) properties of each group of PMMA samples. This study also determined the bending properties (strength, modulus, and maximum deflection at fracture) of each group of PMMA samples from an American Society of Testing Metal (ASTM) standard three-point bend test. This study found that the ENF coating on PMMA significantly improved the surface roughness and cytocompatibility properties of PMMA ( $p < 0.05$ ). This study also found that the bending properties of ENF-coated PMMA samples were not significantly different when compared to those values of the control PMMA samples ( $p > 0.05$ ). Therefore, the PCL ENF coating technique should be further investigated for its potential in clinical applications.

#### 3.2 Background and Significance

Cemented fixation of an implant, used for both osteoporotic and osteoarthritic bone diseases, requires bone cement to hold the implant in place. Although considerable advances have already been made to improve the biological performance of cement, the ideal long-term mechanical stability of a cemented implant has still not been achieved. An ideal cementing material for cemented surgeries should have surface energy and mechanical interlock to ensure a long-lasting fixation between the implant-cement and the cement-bone interfaces [13, 26-28]. The critical task for creating a long lasting tissue-implant interface resides in achieving the

functional integration to mimic the native tissue-tissue failure response [29]. Appropriate mechanical interlock and adequate osseointegration is present between the joining tissues at the natural tissue-tissue interfaces. Since bone cement is a bio-inert material, in the case of the natural tissue-cement interface in a cemented joint, the joining of cement with bone is achieved by mechanical interlock. The goal of this research is to increase the osseointegration at the tissue-cement interface by improving the bioactivity of cement so that it will mimic the native tissue-tissue failure response under functional loading.

Nanofibers are a simple, scalable, inexpensive, and supplementary surface treatment method for biomaterials that have been implemented by various researchers [30-32]. Most research on nanofiber applications with cement is focused on improving the mechanical properties of cement rather than on improving the bioactivity of bone cement. For example, Wagner and Cohn [31] used high performance polyethylene fibers as a reinforcing phase in Poly(methyl methacrylate) (PMMA) bone cement. The authors found that the surface coating treatments of the Spectra 900 polyethylene fibers apparently did not significantly affect the mechanical properties of the PMMA bone cement. Saha and Pal [30] found that the addition of 1%–2% by weight of graphite and up to 6% of aramid fibers into PMMA cement significantly reinforced the mechanical strength of PMMA. However, the previous authors did not conduct cell viability studies to evaluate the effect of their fiber treatments on the biocompatibility of PMMA. Nanofibers can be biomineralised by the immobilization of functional proteins and minerals with the fiber. Wu et al. [33] produced aligned poly(l-lactide)/poly(methyl methacrylate) binary blend fibers and mats loaded with a chimeric green fluorescence protein having a bioactive peptide with hydroxyapatite binding and mineralization properties by pressurized gyration. The previous authors' research showed that nanofibers can have controllable inherent mineralization abilities through integrated bioactivity. The increase of the bioactivity of a bone cement using an electrospun nanofiber coating on cement has not yet been investigated and is pursued in this study.

Electrospinning is a process by which fibers with micron- to nanometer-sized diameters can be deposited on a substrate from an electrostatically driven jet of polymer solution through a needle [34, 35]. These fibers have a high surface area-to-volume ratio, which can be used to produce an electrospun nanofiber (ENF) membrane for biomedical applications [35, 36].

Polycaprolactone (PCL) nanofibers can be produced using an electrospinning process that is biocompatible and nontoxic [35, 37]. We have recently developed a PCL ENF that can control the flow of cement into bone cavities using our patented electrospun nanofiber technology [38]. The effect of the PCL ENF coating on PMMA is not known. A thorough understanding of the PCL ENF coating structure (e.g., topography, thickness) and biomechanical function (cytocompatibility and mechanical responses) relationship in vitro is necessary to evaluate the efficacy of the PCL ENF coating as a functional bio-coating for cemented implant surgery.

The hypothesis of the study is that the PCL ENF coating on cement may increase the biocompatibility of the cement and may lead to better mechanical stability of the cement with the adjoining bone tissue. To test this hypothesis, the first objective of this study was to evaluate the in vitro effects of the PCL ENF coating on the surface topography and cytocompatibility (osteoblast cell adhesion, proliferation, mineralization, and protein adsorption) properties of PMMA bone cement. The second objective of this study was to determine the effect of the PCL ENF coating on the mechanical properties of the PMMA bone cement under three-point bend loading.

### 3.3 Materials and Methods

#### 3.3.1 Materials

A Surgical Simplex<sup>®</sup> P radiopaque bone cement without antibiotic package was used as the PMMA cement. The bone cement package contains 40 gram of PMMA powder consisting of 6 g of polymethyl methacrylate, 30 g of methyl methacrylate-styrene-copolymer (contains benzoyl peroxide and barium sulfate), and 20 mL of liquid that consists of 19.5 mL of methyl methacrylate, *N,N*-dimethyl-para-toluidine, and hydroquinone. PCL pellets (pellet size ~3 mm, average  $M_n$  80,000) and acetone (laboratory reagent  $\geq 99.5\%$ ) were purchased from Sigma Aldrich (Sigma-Aldrich Co., LLC., St. Louis, MO, USA).

#### 3.3.2 Sample Preparation

##### 3.5.2.1 Sample Design

Two groups of samples were prepared for surface topography, mechanical, and cytocompatibility tests to achieve the objectives of this study. The groups are PMMA only

(control) and aligned PCL electrospun nanofiber (ENF) coated PMMA cement, referred to in this article as ENF coated PMMA. The total number of samples tested for confocal, cytocompatibility, and mechanical tests per group are listed in Table 1–3, respectively. The SEM images were captured for only one sample per group.

### 3.5.2.2. Sample Fabrication Process

The process of fabrication for the confocal, cytocompatibility, and mechanical test samples are depicted in **Error! Reference source not found.3-1**. Each step in the fabrication process is explained in the following paragraphs.

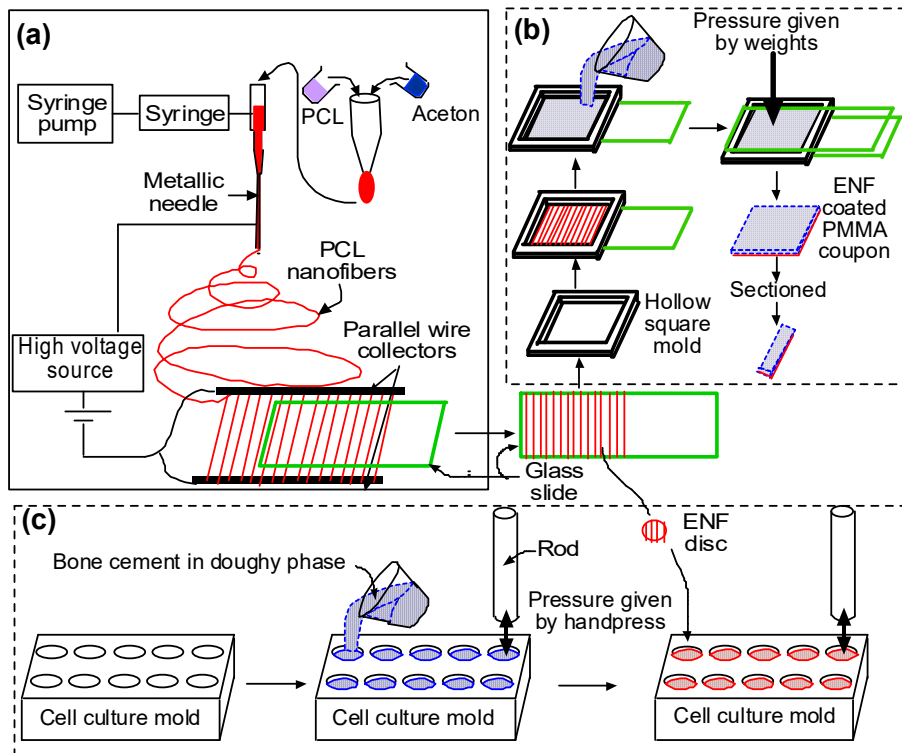


Figure 3-1: Schematic representation of the production methods for (a) single layer aligned PCL ENF production; (b) surface characterization/mechanical test samples; and (c) cytocompatibility test samples.

#### (a) Fiber Production

A glass slide (25 × 75 × 1 mm) was coated with aligned PCL nanofibers using an electrospinning setup. The details of the PCL electrospun nanofiber fabrication can be found in Khandaker and Shahram [24]. In short, PCL pellets (7.69 wt %) were mixed with acetone in an ultrasonic mixer (Sonics & Materials, Inc., Newtown, Connecticut, USA). The sonication

process was carried out at approximately 60 °C for 30 min. The solution was poured into a glass syringe on an infusion pump (Harvard Apparatus, mode # PHD ULTRA) for the PCL fiber production. The PCL solution was ejected from the glass syringe through an electrically-charged needle (23 G blunt needle, 25 mm length, model # BX 25). The needle was positively-charged by a high voltage (15 kV) DC power source (Gamma High Voltage Research, Inc., model # ES 30 series) and two parallel wires were negatively-charged. The aligned PCL fibers were collected between the two parallel wires (Fig 3-2a). To collect multiple layers of aligned fiber, the top surface of the glass slides touched the aligned fiber stream, moved up, and then moved forward to repeat the process to collect 24 layers of fibers (~1.6 micrograms) on the glass sides (Fig 3-2b).

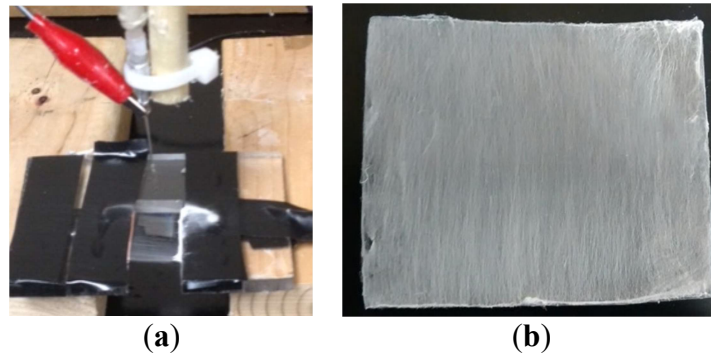


Figure 3-2: (a) Fabrication of aligned PCL fibers for coating using the electrospinning process; (b) Collected fibers on a glass slide.

#### (b) Surface Characterization and Mechanical Test Samples

A glass slide without and with PCL ENF was secured on the bottom of the mold using double-sided tape to prepare the control and ENF coated cement samples, respectively. According to the manufacturer recommendations, the PMMA solution was prepared by hand mixing 2.2 grams of PMMA powder with 1.1 mL of methyl methacrylate (MMA) monomer using a powder:monomer ratio of 2:1. All solutions were cured in a custom-made aluminum mold (Fig 3-3a) to prepare a solid block of PMMA sample of size 25 × 20 × 2 mm. Cement was poured into the chamber of the mold. Another glass side was placed on top of the mold. Weights were stacked on the mold to cure the cement under 60 kPa pressure (clinically applied pressure during orthopedic surgeries [39]). The pressure was initiated at exactly three minutes after the onset of mixing and was sustained throughout the curing period (approximately 15 min) [40]. Figure 3-3b shows a cured control PMMA sample in a mold.

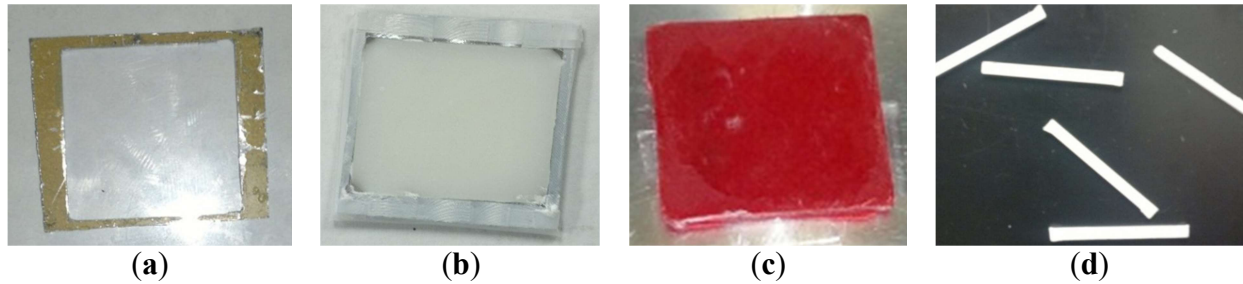


Figure 3-3: (a) Fabricated mold used for curing cement; (b) A cured PMMA cement in the mold; (c) A red dyed ENF coated cement sample on the chamber of the Hitachi TM 1000 scanning electron microscope; and (d) ASTM standard three-point bend PMMA cement specimen.

This study prepared three blocks of control and ENF coated PMMA samples for the mechanical tests. The  $20 \times 25 \times 2$  mm control PMMA blocks were used for both scanning electron microscopy (SEM) imaging and mechanical tests. Mechanical test blocks were also used for the surface topographical analysis using confocal microscopy. Since both PCL ENF and PMMA cement have a white color, this study prepared separate  $20 \times 25 \times 2$  mm ENF coated PMMA blocks for SEM imaging and mechanical tests. To prepare an ENF coated PMMA sample for SEM imaging, the PMMA solution was mixed with a red-colored dye before being poured into the mold. Figure 13c shows ENF coated PMMA samples that were used for SEM analysis. To prepare ASTM F417-78 standard flexural [41] test samples, ( $20 \times 4 \times 2$ ) mm blocks were cut from the ( $20 \times 25 \times 2$ ) mm block using a Buehler Isomet low-speed cutter. A ( $102 \times 0.31 \times 12.7$ ) mm wafering blade was used for cutting the samples. Figure 3-3d shows the PMMA samples that were used for the mechanical tests. The samples were stored in cell culture flasks at room temperature for SEM analysis and mechanical tests.

### (c) Cytocompatibility Test Samples

Cytocompatibility properties (osteoblast cell adhesion, proliferation, mineralization, and protein adsorption) of the control and ENF coated PMMA samples were conducted in a custom made well. PCL ENF were collected between the wires until a fibrous cloth appeared. A 10 mm diameter PCL fiber disc was cut from the cloth using a punch (Fig 3-4a). PMMA specimens were prepared by mixing 0.5 grams of PMMA beads with 0.25 mL of MMA. All PMMA samples, while still pliable, were divided into 4 parts by a knife and were poured in the well. Each part of the samples was hand pressed during curing by a flat-ended 9.565 mm diameter highly polished round bar. The round bar has clearance fits on the wells of the well plate. To

prepare the ENF coated PMMA sample, a 10 mm diameter PCL fiber disc was placed on the cement and again pressed by the round bar to attach the PCL fiber on the top of the PMMA. The sample wells were kept sterile in a biological safety cabinet under ultraviolet (UV) light for subsequent cell culture.

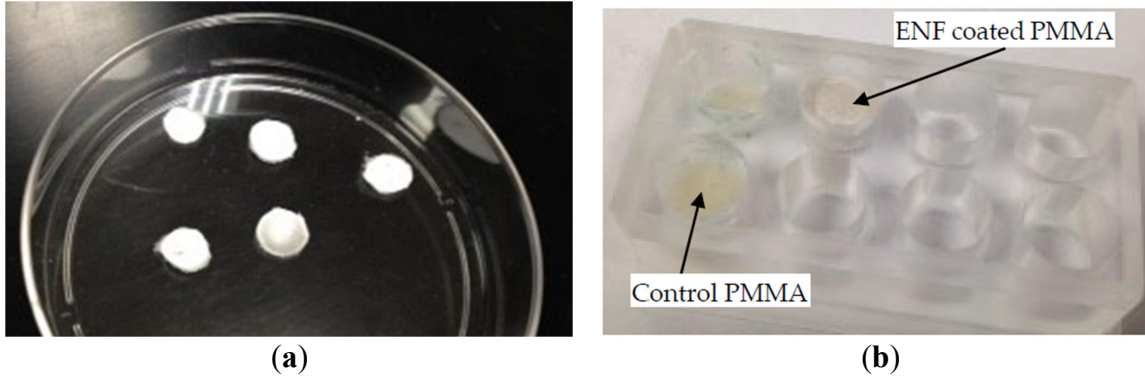


Figure 3-4: (a) ENF discs which were pressed on the top of PMMA during the doughy phase of the cement; (b) Control and ENF coated PMMA samples in an acrylic mold which were used for cytocompatibility tests.

### 3.4 Experiments and Analysis

#### 3.4.1 Surface Topography

Surface topography is an important parameter that plays a significant role in implant-bone adhesion. The influence of the ENF treatment on the surface morphology of PMMA was evaluated by a Keyence VK laser confocal microscope using 50× brightfield conditions. Scanning was conducted over 287.32  $\mu\text{m}$  length  $\times$  214.93  $\mu\text{m}$  width  $\times$  11.14  $\mu\text{m}$  height for all samples. Topography images were compared for three control and ENF coated PMMA samples. Roughness parameters ( $R_a$ ,  $R_z$ , and  $R_{sum}$ ) were directly measured from the line and surface scanning for the captured images [42].

#### 3.4.2 Cell Adhesion, Proliferation, Mineralization, and Protein Adsorption Tests on PMMA

##### Samples

Rat osteoblast cells (R-OST-583; Lonza) were cultured at log phase growth in standard culture conditions (37 °C in a 5% CO<sub>2</sub> incubator on tissue culture dishes) using DMEM/high glucose + 5% FBS and 1% ABAM (Sigma Chemical). Cells were dissociated using 1× trypsin/EDTA solution (Sigma Chemical) for 5 min at room temperature, followed by serum inactivation. Cells were counted using a hemocytometer, collected by centrifugation, and re-



suspended at a concentration of 25,000 cells per 400 microliters of growth media as the custom-made acrylic well capacity was 400 microliters. Osteoblast cells were seeded at a density of 25,000 cells/well on each group of PMMA samples in a custom-made silicone well-plate. Cells were then cultured for 48 h to allow cell adhesion and proliferation on the PMMA surface. Parallel samples similar to those tested for adhesion and proliferation were cultured for 3 weeks and prepared for immunostaining to determine hydroxyapatite mineralization and osteonectin adsorption. A Click-iT<sup>®</sup> EdU stain was used to evaluate cell adhesion and proliferation for each sample according to the vendor's protocol [43]. This 48-h assay involved the addition of EdU, or 5-ethynyl-2'-deoxyuridine, to each well after the initial 24 h incubation. The EdU was a modified thymine nucleotide that contained a terminal alkyne. After a total of 48 h, the cells were fixed with paraformaldehyde and stained with Alexa-488. The terminal alkyne in the EdU reacted with the azide in Alexa-488, which caused the proliferated cells that incorporated the EdU tag to fluoresce green under fluorescent microscopy. An OsteoImage<sup>™</sup> mineralization assay kit from Lonza was used according to the vendor's protocol. For the protein adsorption test, anti-osteonectin (clone AON-1; Developmental Studies Hybridoma Bank) was used as the primary antibody and goat anti-mouse rhodamine (red) was used as the secondary antibody. For the mineralization and protein adsorption tests, nuclei were stained with Hoechst stain (blue). The qualitative and quantitative measurements of cell viability on the ENF treated PMMA surfaces were conducted from images captured with an Olympus DP72 camera and CelSens software. Cell adhesion on the surface of all types of PMMA samples was analyzed for the qualitative measurement of cell viability. The number of cells adhered and the number of cells proliferated after adhesion to each sample were determined from the captured images using the ImageJ software program (<http://imagej.nih.gov/ij/>) (National Institutes of Health, Bethesda, Maryland, USA). Cell densities on ENF coated PMMA samples were compared with the control PMMA samples for the quantitative measurement of cell adhesion and the percentage of proliferation. The ratio of mineralized and osteonectin stain area over the total area of the image field was used to compare the mineralization and osteonectin activities between the control and ENF coated PMMA samples, respectively.

### 3.4.3 Mechanical Tests

Three-point bend (3PB) tests were conducted on each group of PMMA samples ( $n = 10$ ) to compare the bending modulus, strength, and maximum deflection between the sample groups. Each sample was tested at room temperature at the loading rate of 0.01 mm/s using a Test Resources Universal Testing Machine. The specimens were mounted on the custom-made roller supports (span length = 16 mm) in the test stage and were pressed by a custom made 3PB indenter (tip radius = 3.2 mm) (**Error! Reference source not found.**). The load vs. displacement was continuously recorded until the failure of the specimens. The corresponding stress-stress values from the load-displacement values and the bending properties were calculated using ASTM F417-78 standard formulations [41].



Figure 3-5: Three-point bend fixture for determining the bending properties of the bone cement.

### 3.4.4 Statistical Analysis

Independent sample  $t$ -tests, assuming unequal variances, were used to test for differences in mean adhesion density, cell proliferation, mineralization, amount of osteonectin, roughness, width, height, bending modulus, bending strength, and maximum deflection between the control and ENF coated PMMA samples. To test for differences in the mean number of adhered cells after 2 and 14 days, a two-factor (time and treatment) analysis of variance (ANOVA) was performed. Due to the presence of one extreme outlier and an indication of heterogeneity, ANOVA was performed on the log transformed data. A significance level of 0.05 was used for

all tests. All analyses were performed using either proc *t* test or proc mixed in SAS v. 9.4 (SAS Institute, Cary, North Carolina, USA).

### 3.5 Results

#### 3.5.1 Surface Topography

A clearly visible difference in surface topography was observed from SEM (Fig 3-6) and confocal microscope images (Fig 3-7) between the control and ENF coated PMMA samples. Significant differences in mean roughness parameters were observed between the sample groups ( $p$ -value  $< 0.05$ ) (Table 3-1). This result suggested a significant change of the surface texture due to the ENF treatment. The overlapping of multiple fibers was observed in the ENF coated PMMA samples (Fig 3-6b). The fiber thickness calculated from the SEM images of the ENF coated samples was found to be in the range from 0.432 to 0.648  $\mu\text{m}$ . The 2D and 3D confocal topography images of the ENF coated PMMA samples showed that the direction of ENF deposition was mainly uni-directional, although it was not possible to measure the quality of the fiber alignment for the images due to embedding of the fiber into the PMMA cement. It is clear from comparing the confocal images between the control and ENF coated PMMA samples that the visibility of PMMA beads increased due to the deposition of ENF on the PMMA cement.

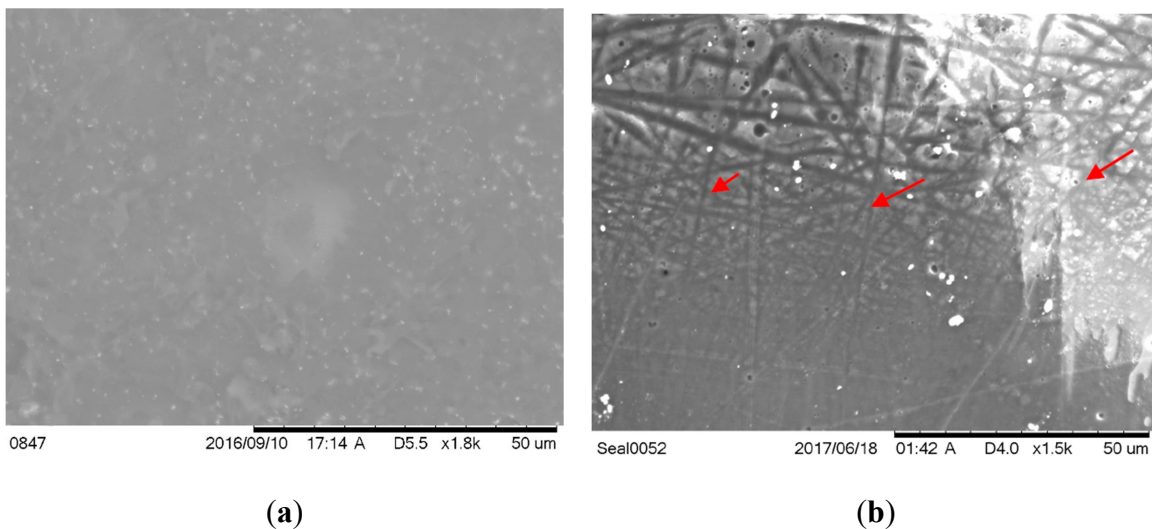


Figure 3-6: Scanning electron microscope images of the (a) control and (b) electrospun nanofiber (ENF) coated Poly(methyl methacrylate) (PMMA) specimen.

The red arrows in Figure 3-5b show the embedded single Polycaprolactone (PCL) ENF in the ENF coated PMMA specimen.

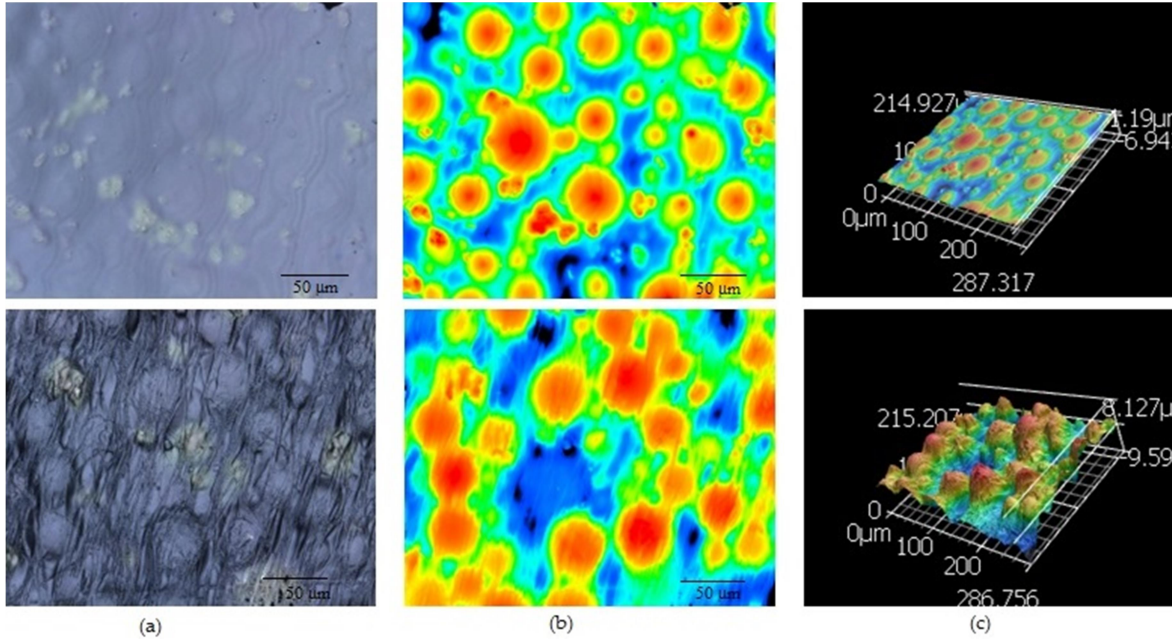


Figure 3-7: Confocal microscope images of a control (top row), and ENF coated PMMA (bottom row) sample: (a) 2D topography; (b) height amplitude mapping; and (c) 3D topography images. The length of the scale bar is 50 micrometers in the figures of column (a,b). The magnification of column (c) images is 20 $\times$ .

Descriptions	Control	ENF Coated	<i>t</i>	<i>p</i> -value
$R_a$ ( $\mu\text{m}$ )	$0.26 \pm 0.03$	$2.75 \pm 0.17$ **	14.82	0.003
$R_z$ ( $\mu\text{m}$ )	$1.45 \pm 0.25$	$14.13 \pm 1.24$ **	10.02	0.008
$R_{\text{sum}}$ ( $\mu\text{m}$ )	$75.47 \pm 3.57$	$102.00 \pm 6.30$ *	3.66	0.032

Table 3-1: Difference of roughness between control and electrospun nanofiber (ENF) coated Poly(methyl methacrylate) (PMMA) samples. Data are presented as mean  $\pm$  standard error. Data are presented with  $n = 3$  for both samples. Note:  $p < 0.05$  is denoted by \* and  $p < 0.01$  by \*\* (compared to control).

### 3.5.2 Cytocompatibility Properties

Cell adhesion and proliferation successfully occurred on the surface of the control and ENF coated PMMA samples, as shown in Figure 3-7: A representative fluorescent stained image (100 $\times$  total magnification, scale bar = 500  $\mu\text{m}$ ) from adhesion and proliferation assays showing adhered (blue color) and proliferated cells (green color) of the (a) control and (b) ENF coated PMMA samples.

-8. There was a significant difference in the mean cell densities (combined blue and green nuclei) of the control and ENF treated PMMA sample groups observed with time ( $F_{1,56} = 16.18$ ,  $p$ -value  $< 0.001$ ) (Table 3-2). Both samples demonstrated adhered cell nuclei (blue color Hoechst stained) and proliferating cell nuclei (green color edu-click stained). Cells grew more readily on fibrous samples in ENF coated PMMA samples and with increased cluster distribution along the surface of the fibers on the ENF coated PMMA surface compared to the control ( $p$ -value  $< 0.001$ ). Although the mean number of cells proliferating on the PMMA surface was higher for the ENF coated PMMA samples compared to the control samples, there was no significant difference in the mean percentage of cell proliferation between the samples ( $p$ -value = 0.297) as shown in **Error! Reference source not found.3.8**. These results suggest that the ENF coating may have a positive influence on the in vitro osseointegration with the PMMA surface.

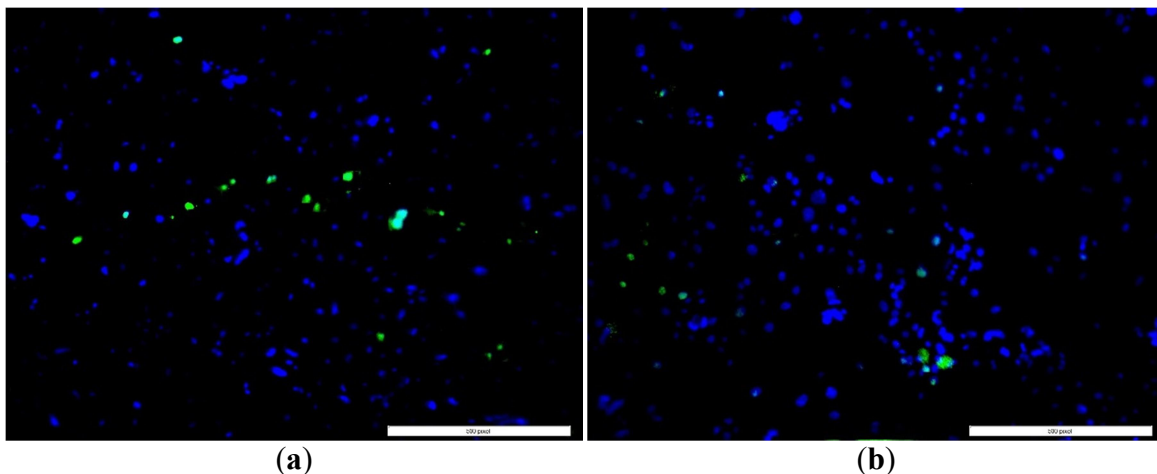


Figure 3-7: A representative fluorescent stained image (100 $\times$  total magnification, scale bar = 500  $\mu$ m) from adhesion and proliferation assays showing adhered (blue color) and proliferated cells (green color) of the (a) control and (b) ENF coated PMMA samples.

Parameters Descriptions	Control	ENF Coated	$F_{1,56}$	$p$ -value
No. of adhered cells after 2 days of cell culture	232 $\pm$ 16	309 $\pm$ 12 *	6.01	0.018
No. of adhered cells after 14 days of cell culture	428 $\pm$ 53	615 $\pm$ 65 **	10.48	0.002

Table 3-2: Summary statistics for the cell viability tests with respect to the cell culture time by sample group. Data are presented as mean  $\pm$  standard error. Data are presented with n = 28 for both samples. Note: p < 0.05 is denoted by \* and p < 0.01 by \*\* (compared to control).

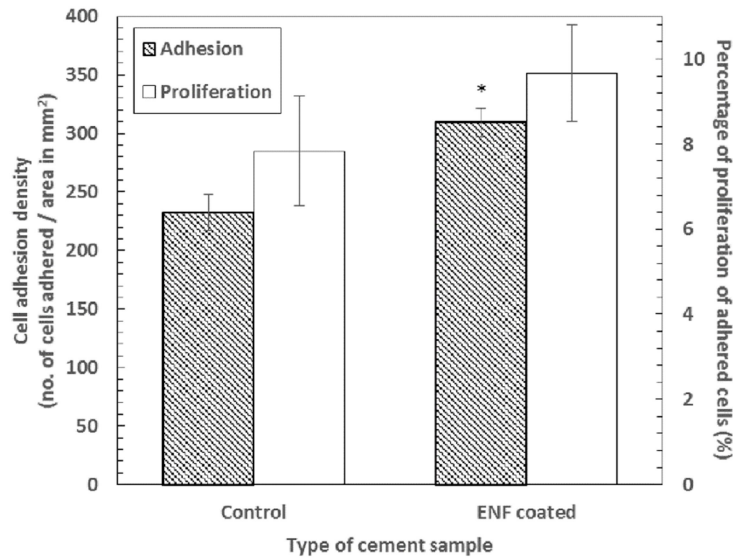


Figure 3-8: Mean cell adhesion density ( $\pm$  standard error) and the percentage of cell proliferation ( $\pm$  standard error) for the control and ENF coated PMMA groups after 48 h of cell culture. Data are presented with n = 14 for both samples. Note: \* p < 0.05 (compared to control).

Cell mineralization and protein adsorption successfully occurred on the surface of all types of PMMA samples as shown in Figure 3-9 and Figure 3-10. Both samples demonstrated adhered cells (blue nuclei) and hydroxyapatite mineralization from the cells (green stained). Although the study found a low amount of mineralization for both the control (0.18–11.32%) and ENF coated PMMA (0.39%–10.79%) samples, the mean number of cells mineralized after adherence to the PMMA surface was higher for the ENF coated PMMA samples compared to the control samples, and there was no significant difference in the mean amount of mineralization (total green stained area  $\times$  100%/area of image field) of the control and ENF treated PMMA sample groups (p-value = 0.228) (Fig 3-11). Both samples demonstrated adhered cells (blue nuclei) and the presence of osteonectin from the cells (red stained). There was a significant difference in the mean amount of osteonectin (total red stained area  $\times$  100%/area of image field) between the control and ENF treated PMMA sample groups (p-value = 0.008) (Fig 3-11). The result suggested that the inclusion of ENF has a positive effect on the cytocompatibility properties of PMMA.

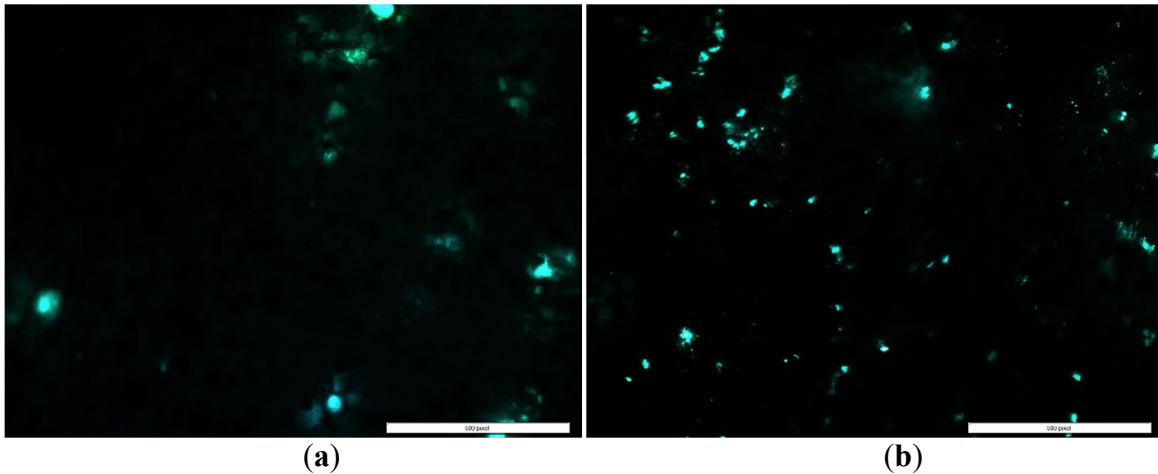


Figure 3-9: A representative fluorescent stained image (100× total magnification, scale bar = 500  $\mu\text{m}$ ) from the mineralization assays showing the released mineral (green) from the cells of the (a) control and (b) ENF coated PMMA samples after 3 weeks of cell culture

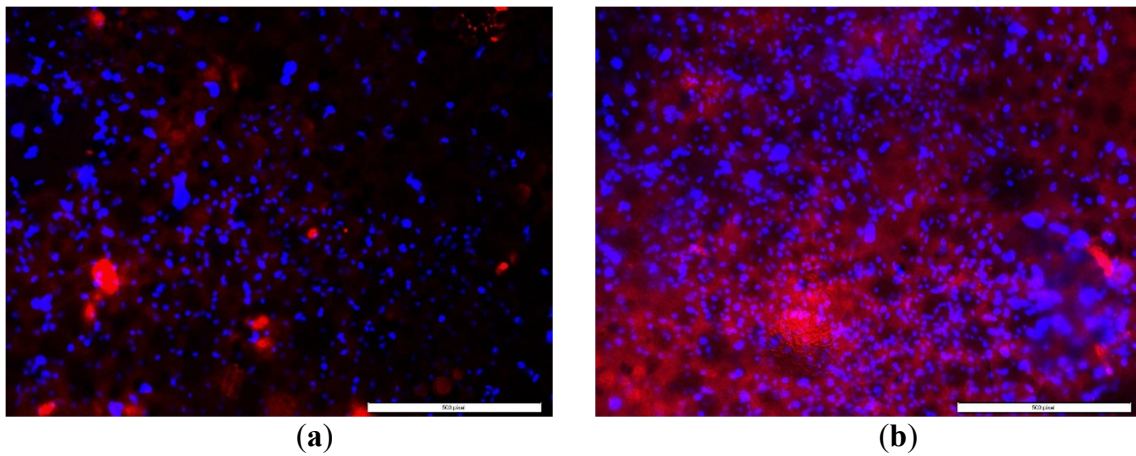


Figure 3-10: A representative fluorescent stained image (100× total magnification, scale bar = 500  $\mu\text{m}$ ) from the protein adsorption assays showing osteoblast nuclei (blue) and released osteonectin (red) from the cells of the (a) control and (b) ENF coated PMMA samples after 3 weeks of cell culture.

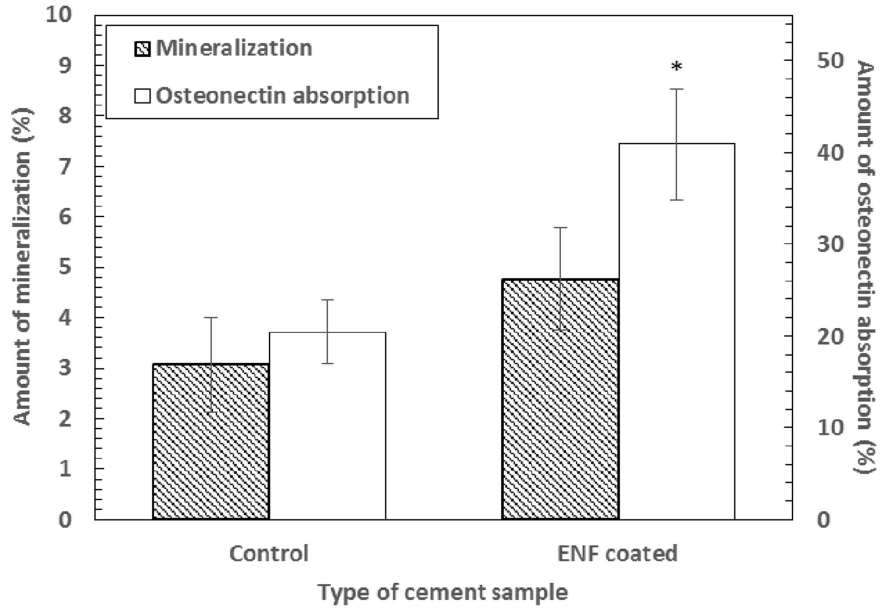


Figure 3-11: Mean amount of mineralization ( $\pm$  standard error) and mean amount of osteonectin ( $\pm$  standard error) for the control and ENF coated PMMA groups. Note: \*  $p < 0.05$  (compared to control).

### 3.5.3 Mechanical Tests

There was negligible difference of the stress-strain behavior between the control and ENF coated samples (**Error! Reference source not found.**). The stress-strain curves for both samples can be characterized as an initially elastic response, followed by a short inelastic region and then a sudden descending response due to failure of the specimen. **Error! Reference source not found.**-3 summarizes the bending strength,  $\sigma_f$ , bending modulus,  $E$ , and maximum deflection of the control and ENF coated PMMA samples. Although the mean value for each of the experimental parameters under bending load was different between the ENF coated and control PMMA samples, the difference was not statistically significant ( $p$ -value  $> 0.05$ ).



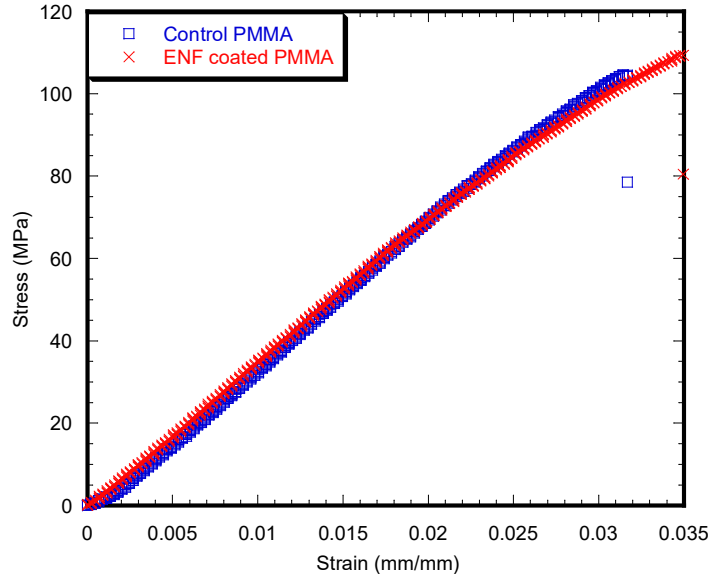


Figure 3-12: Typical stress vs. strain plots of the control and ENF coated PMMA specimens. The observed difference between the maximum stress and strain values in the figure is due to the difference of the dimensions and internal structures of the samples.

Parameters Descriptions	Control	ENF Coated	<i>t</i>	<i>p</i> -value
Width of the sample	1.97 ± 0.01	1.98 ± 0.03	0.23	0.83
Height of the sample	1.49 ± 0.01	1.51 ± 0.01	1.31	0.20
Bending modulus (GPa)	3.32 ± 0.11	3.30 ± 0.07	0.15	0.88
Bending strength (MPa)	106.97 ± 4.94	108.12 ± 3.05	0.20	0.85
Maximum deflection (mm)	1.56 ± 0.07	1.58 ± 0.04	0.15	0.88

Table 3-3: Summary statistics for the three-point bend test experimental data by sample group. Data are presented with  $n = 10$  for both samples. Data are presented as mean ± standard error. Note: \*  $p < 0.05$  (compared to control).

### 3.6 Discussion

The topographical analysis results (Fig 3-5 and Fig 3-6 and Table 3-1) suggested that the inclusion of ENF has a significant effect on the surface morphology of PMMA. There was variability in the amount of fiber deposition, alignment, and diameter of the fiber along the ENF coated PMMA surface. This variability happened due to the variation of the fiber production and manual collection process. The topographical difference among the ENF coated PMMA samples led to a higher amount of variance (represented by the standard error) in roughness parameters for the ENF coated PMMA samples compared to the control samples (**Error! Reference source not found.**). To reduce the effect of the fiber topography on the cytocompatibility and mechanical test results for the ENF coated PMMA samples, fibers were deposited on the parallel wire collectors for the same time period under the same fiber production conditions (PCL

solution viscosity, DC voltage, and solution flow rate). An automated fiber collection process from the parallel wire collectors is required to further minimize the effect of topographic variation on the cytocompatibility and mechanical test results of the ENF coated PMMA samples.

The ENF coated PMMA samples demonstrated better biological responses compared to non-treated PMMA samples. Over the three-week period of in vitro culture, osteoblasts persisted, proliferated, and differentiated on the PMMA substrate in the presence and absence of ENF. The adhesion and proliferation test results of control PMMA samples were similar to our previously published report [44]. The mean percentage of proliferation in the control versus ENF coated PMMA was not significantly different. This suggests that the rate of proliferation was constant in both treatments. However, more cells were clearly present in clusters for the ENF coated PMMA compared to the control (Figure 3-7: A representative fluorescent stained image (100× total magnification, scale bar = 500 μm) from adhesion and proliferation assays showing adhered (blue color) and proliferated cells (green color) of the (a) control and (b) ENF coated PMMA samples.

). Two hypotheses can be provided for this response: (1) When cells were initially plated, they adhered better to the ENF matrix and therefore more cells were present initially; or (2) Cells were dying at a greater rate in PMMA compared to the ENF coated PMMA. Neither of these hypotheses were tested here, but would be interesting to study in the future.

Osteoblast cell differentiation was demonstrated by calcium phosphate mineral (Figure 3-9: A representative fluorescent stained image (100× total magnification, scale bar = 500 μm) from the mineralization assays showing the released mineral (green) from the cells of the (a) control and (b) ENF coated PMMA samples after 3 weeks of cell culture

) and osteonectin expression from fluorescent stained images (Figure 3-10: A representative fluorescent stained image (100× total magnification, scale bar = 500 μm) from the protein adsorption assays showing osteoblast nuclei (blue) and released osteonectin (red) from the cells of the (a) control and (b) ENF coated PMMA samples after 3 weeks of cell culture.

). While both mineralization and osteonectin expression increased with the ENF treatment, the increase of mineralization was not found to be statistically significant for the ENF coated PMMA group compared to the control (**Error! Reference source not found.**). The study found a low percentage amount of mineralization for both the control and ENF coated PMMA samples.

This is due to the fact that the study conducted the mineralization assay after 14 days of cell culture on the samples according to the vendor recommendation (OsteoImage™ mineralization assay kit from Lonza). Since the amount of mineralization from the adhered cells are highly dependent on the period of cell culture [45, 46], more culture time is therefore required to obtain a higher amount of mineralization.

In this study, we observed increased cytocompatibility properties (adhesion, proliferation, and protein adsorption) of the ENF coated PMMA implants compared to PMMA. This is because higher cell functions were created via better cell signaling arising from the cell-cell contact and the cell-ENF components in the ENF coated PMMA samples. Cell signals depend upon the physical (micro- or nano-structured surface topography, composition of ENF) and chemical properties of ENF. There exists differences of the physio-chemical properties between the control and ENF coated PMMA samples. The PCL nanofibers on PMMA lead to different physical characteristics viz. porosity and density due to the distribution of the PCL fiber. PCL in the ENF coated PMMA created a larger surface area that provided more cell binding sites. Additionally, PCL ENF can absorb numerous proteins or minerals akin to a cell membrane receptor, thus favoring cytocompatibility properties for the ENF coated PMMA samples compared to the control.

PMMA is a bio-inert material. The purpose of coating PMMA at the bone/cement interface was to improve the biocompatibility of the PMMA cement without diminishing the mechanical properties of PMMA in in vivo conditions. The stress-strain behavior (**Error! Reference source not found.**) and the measured mechanical properties (**Error! Reference source not found.-3**) of the PMMA and ENF coated PMMA samples suggested that the inclusion of ENF has no statistically significant effect on the mechanical property of PMMA under three-point bend loading. Therefore, the PCL ENF membrane can potentially be used as a functional bio-coating material for PMMA. Since the PCL ENF membrane has negligible strength ( $E = 10.2\text{--}27.3$  MPa and  $\sigma_f = 1.5\text{--}3.6$  MPa [47]) compared to PMMA, it has a negligible impact on the increase of the strength of PMMA. An alternative high strength electrospun nanofiber material such as Polycaprolactam (nylon 6), or graphene oxide-based nanofibers can be used with PMMA for the combined improvement of mechanical and biological properties. The mechanical properties of PCL ENF depended highly upon the number of electrospun layers. This study used only 24 layers of fiber (negligible weight compared to the weight of the PMMA block) to coat the

PMMA for the mechanical test samples. A large amount of PCL ENF is required to improve the elasticity of PMMA.

This study was motivated by a clinical problem where the heterogeneous flow of bone cement around the implants to the adjacent bone tissue has been observed due to the porosity of bone [38]. Since significantly more cracks are associated with the interdigitated area and the cement/bone interface than with the implant/cement interface [19], there is a high probability that localized fractures may occur at the narrowly confined cement/bone interfaces [20] due to this heterogeneous flow of cement. The goal of reducing the localized fractures due to the heterogeneous flow of bone cement at the tissue-cement interface by a functional nanofiber coating on cement has been investigated in a separate study.

The method of coating the bone cement by the ENF membrane can be applied in clinical fields for the fixation of implants in bone using PMMA. For a case of cemented implant fixation, an electrospinning process (patent pending) has been used in our study to create a cylindrical PCL ENF cup by electrospinning PCL on a round shape collector [38]. In our in vivo study, we have inserted the PCL ENF cylindrical cup into the hole of a rabbit femur at the epiphyso-metaphyseal junction. The cement in the dough phase of mechanical properties during the polymerisation process was injected into the hole of the ENF cup by a syringe. Subsequently, the implant was hand-pressed into the cement. Due to the high flexibility and porosity of the ENF cup, the cement with ENF anchored with the bone. Our patent pending method [48] can also be applied to a cemented hip implant, where the shape and size of the ENF membrane can be the same as the shape and size of the hole drilled for the anchor of the cemented hip implant. Our invented ENF cup succeeded in holding the cement, which was confirmed from mechanical and histological tests. The results of the mechanical and histological tests will be presented in a separate manuscript.

To our knowledge, this is the first study to evaluate the effect of an aligned PCL ENF coating treatment on the cytocompatibility of PMMA using osteoblast cells and flexural properties of PMMA cement. However, the value of the  $R_a$  of PMMA ( $0.26 \pm 0.03 \mu\text{m}$ ) in this study is in close agreement with the  $R_a$  of PMMA ( $0.37 \pm 0.09 \mu\text{m}$ ) found by Moursi et al. [49]. The values of the mechanical and cytocompatibility properties of PMMA in this study are different than those values of PMMA in our previous study [44], likely because we used two

different brands of PMMA cement. Cobalt <sup>HV</sup> bone cement was used in our previous study, whereas Stryker Simplex<sup>®</sup> P bone cement was used in this study. Due to the ease of sample preparation, this study was limited to only bending tests on the test samples to measure the effect of the PCL nanofibers on PMMA. Another reason for using flexural testing is that it is more sensitive to surface effects than tension and compression.

This study is limited to the production of PCL nanofibers by an electrospinning method and blending of the produced PCL ENF with PMMA bone cement. There are several other methods, such as pressurized gyratory spinning [50] and pull spinning [51], which can be used to produce a PCL nanofiber membrane for the coating of bone cement. The capability of electrospinning to function as an automated, scaled, and point-of-use fiber manufacturing platform was demonstrated by Khandaker and Shahram [52]. There might be positive and negative consequences from using each of the above methods for the rapid coating of bone cement with nanofibers, which would be a potential area of investigation related to this research. This study is limited to the use of PCL nanofibers as the coating material. The reason for selecting PCL ENF among many other biocompatible and degradable nanofibers is that PCL can be immobilized with osteoconductive biomolecules, antimicrobial nanoparticles, growth factors, and proteins. The blending of protein and mineral immobilized fibers with PMMA cement can further improve the bio-functional properties of PMMA cement. Another limitation of the study was that the mechanical tests were conducted on samples kept at room temperature. However, bone cement undergoes polymerization due to the inclusion of a system that generates free radicals, but once in the body further polymerization occurs due to the body temperature, thus the cement should have been left in saline or cell culture fluid for a week at 37 °C before mechanical testing to allow the cement to be set as it would be in the body. Considering the fact that there is no effect of the PCL ENF coating on PMMA, and that PCL fiber is degradable, it is anticipated that keeping the samples at 37 °C in a phosphate buffer solution would have no effect on the mechanical properties. Further research is required to verify this anticipation.

The cytocompatibility properties of nanoparticle (MgO, hydroxyapatite, chitosan, BaSO<sub>4</sub>, SiO<sub>2</sub>) incorporated PMMA was explored in our earlier study [44]. Several researchers were able to attach drugs (e.g., collagen [53], ampicillin [54], resveratrol [32], hydroxyapatite [55]) with nanofibers. The combined application of nanoparticles and nanofibers blended on PMMA can further enhance the biocompatibility of PMMA, which is a potential area of new research.

### 3.7 Conclusions

This study found a statistically significant improvement on the osteoblast cytocompatibility properties of PMMA for PCL ENF treated PMMA samples compared to the non-treated PMMA samples due to the increased PMMA cement surface roughness. In addition, this study observed that the PCL ENF coating on PMMA had no adverse effect on the mechanical properties of PMMA under bending. Since the PCL ENF coating method developed in this study improved the physico- and biocompatibility of PMMA, it can be concluded that PMMA surface modifications by PCL ENF coating favor in vivo bone formation that leads to improved implant union with bone.

**Acknowledgement:** I would like to acknowledge Sharam Riahanizad and Alexi Coles at the University of Central Oklahoma for the above collaborative work.

## CHAPTER 4

### IMMOBILIZATION AND CHARACTERIZATION OF METAL OXIDES IN AN ELECTROSPUN NANOFIBER MEMBRANE FOR GAS DETECTION

#### 4.1 Summary.

Innovation and relatedness of the project in the fields of climate variability. Gas environment detection has become more urgent and significant for environment monitoring from climate variability. Gas sensors based on a catalytically-sensing mechanism are one of the most important types of devices for gas detection, and have been an active area of research. However, even though many efforts have contributed to this area, some great challenges still remain, such as the development of sensitively and selectively sensing catalysts. Different metal oxides catalysts (such as MgO, TiO<sub>2</sub>, ZnO) in form of nanoclusters can be loaded to polymeric nanofiber surface to detect gas with high precision [56]. The metal oxide nanoparticles (MO-NPs) can be assembled with the ultrafine fibers produced via electrospinning as a three-dimensional structured fibrous membrane with controllable pore structure and high specific surface area to produce a membrane that can be used as a precision gas sensing device. This project will develop electrospun nanofiber based sensing technologies that fill gaps in current operational capabilities of gas sensors.

#### 4.2 Goals and Objectives.

The goal of this project is to immobilize three different metal oxide (MO) nanoparticles (NPs) (MgO, TiO<sub>2</sub>, ZnO) with polycaprolactone (PCL) nanofiber membrane (NFM) to create MO-PCL NFM for the fabrication of highly sensitive gas sensors for the applications in climate variability research. The major objectives of this research are: (1) to immobilize the MOs with the PCL NFM, (2) to determine the structure and morphology of the MO-PCL-NFM by scanning electron microscopy (SEM), Energy Dispersive Spectroscopy (EDS), X-ray diffraction (XRD) and Fourier transform infrared spectroscopy (FTIR) and (3) to explore the feasibility of using each of MO-PCL NFM for the design of a specific gas sensor.

### 4.3 Background and Significance.

Sensing material is commonly the key part of the gas sensor. Therefore, the development of sensors mainly focuses on exploring high-performance sensing materials. Metal oxide nanomaterials are widely used to fabricate efficient gas sensors for the detection of various hazardous and toxic gasses. For example, MgO is used for SO<sub>2</sub> gas sensors [4], TiO<sub>2</sub> NP is used for low-temperature CO<sub>2</sub> gas sensors [5], ZnO NP is used for NO<sub>2</sub> gas sensors [6]. Electrospinning is a process by which organized fibers of micron- to nanometer diameters can be deposited on a substrate from an electrostatically-driven jet of polymer solution through a needle. Electrospun PCL nanofibers having a high surface area-to-volume ratio can be used as a carrier for MO-NPs for gas sensing applications. The effect of the immobilization of each of the MOs with PCL and characterization is significant for developing highly sensitive gas sensor due to climate change.

### 4.4 Experimental Design and Methods.

Four groups of NFM will be fabricated: PCL NFM (control), MgO NPs immobilized PCL NFM (referred as mPCL NFM), ZnO NPs immobilized PCL NFM (referred as zPCL NFM) and TiO<sub>2</sub> NPs immobilized PCL NFM (referred as tPCL NFM). PCL NFM will be produced according to our previously developed method [57]. PCL solutions with different types of MO NPs will be dissolved in acetone. Briefly, a 5 wt. % of each kind of NPs will be accurately weighed and sonicated for 30 minutes to properly disperse in acetone. Then, PCL beads will be added to the above solution so that the final solution contains 15 wt.% PCL, and the mixture will be stirred with a magnetic stirrer for 12h to ensure the dissolution of the pellets and proper mixing. About 10ml of the prepared solutions with each group of a MO-PCL solution will be taken in glass syringes and electrospun individually on two parallel plate collectors to produce aligned MO-PCL NFM. To collect multiple layers of fiber, an acrylic hollow cylindrical substrate will be used to touch the aligned fiber stream, then lower it and rotate the substrate 90° and repeat the process to collect another layer. The process will be repeated 24 times to create each group of MO-PCL NFM. All groups of samples will be produced at UCO. SEM analysis will be performed on each samples using OSU facilities.



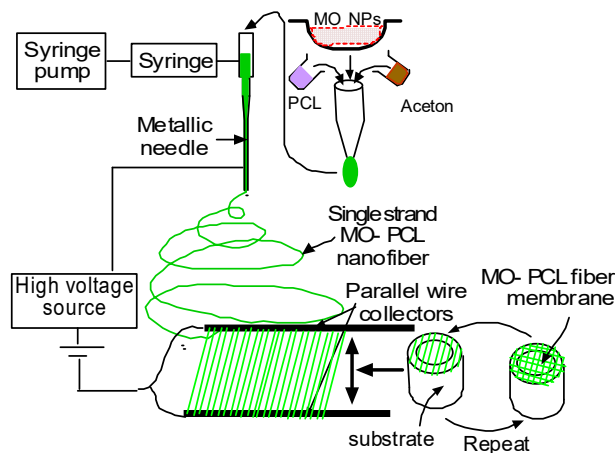
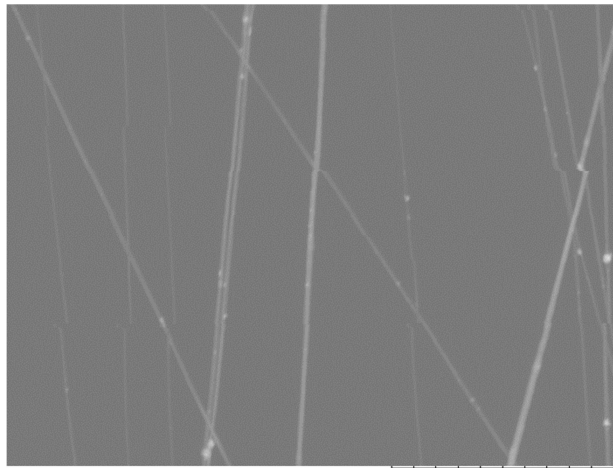


Figure 4-1 Schematic image of the creation of MO-PCL NFM

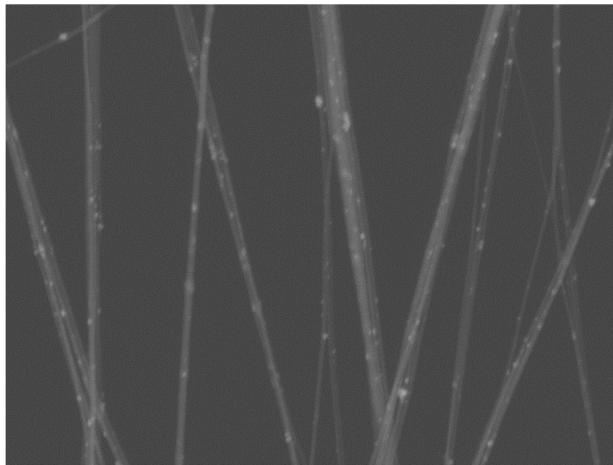
#### 4.5 Results and Discussion.

Dr. Khandaker research group developed an electrospun nanofiber production technique [52], by which a single strand of PCL nanofiber can be deposited between two parallel wire collectors (**Error! Reference source not found.**). The group also conducted a preliminary study to examine whether each of the MO NPs can be tethered with a single PCL nanofiber using the electrospun unit. A PCL solution with each of the MO NPs is loaded into the syringe and this liquid is extruded from the needle tip at a constant rate by a syringe pump. The needle and wire collectors are positively and negatively charged, respectively. The path of an electromagnetic field generated by the potential difference between the charged needle and the collectors is used to deposit and align fiber on the collector. These fibers when harvested at different angles and stacked in layers to produce each of the MO NPs added NFM on an acrylic substrate. Our preliminary experiment shows that it is possible to tether each of the MO NPs with PCL nanofiber using our electrospun process. The scanning electron microscope image showed tethered MO NPs with PCL (**Error! Reference source not found.**). The diameter of a fiber, gap size between adjacent fibers, and alignment of fibers in the fabricated membranes was observed by SEM. EDS analysis confirmed that MO NPs reached the collector along with the polymer solution during the electrospinning process and structure of the nanomaterials (fibers and particles). Further structural and morphological analysis is required to understand the chemical, ionic, structural forms and shapes of the MO NPs in the PCL NFM for evaluating the feasibility of the MO-PCL NFM for its application in gas sensor.



Seal0166 2017/07/24 22:33 A D5.6 x1.2k 50 um  
Time Set 2 Sample

(a)



Seal0169 2017/07/25 01:32 A D8.6 x1.2k 50 um  
Time Set 2 Sample

(b)

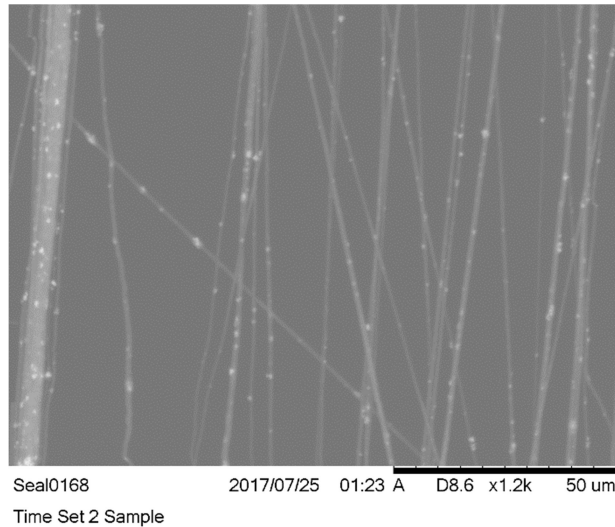


Figure 4-2: SEM image showing the presence of MgO NPs in a PCL fiber: (a) MgO, (b) ZnO and TiO<sub>2</sub> NPs added PCL.

(c)

#### 4.6 Future works.

XRD will be used to understand the crystallinity and the structure of the fabricated materials. FTIR will indicate the range of transmittance and interaction between the carbonyl groups of PCL with the MO NPs. The results will be analyzed to determine the feasibility of using each of MO-PCL NFM for the design of a specific gas sensor device.

## CHAPTER 5

### **Evaluation of Polyethylene Glycol Diacrylate-polycaprolactone scaffolds for a tissue engineering application**

#### 5.1 Summary

Polyethylene Glycol Diacrylate (PEGDA) tissue scaffolds having thickness higher than 1 mm and without the presence of nutrient conduit networks were shown to have limited applications in tissue engineering due to the inability of cells to adhere and migrate within the scaffold. The polycaprolactone (PCL) electrospun nanofiber (ENF) membrane can be subsequently coated with PEGDA to overcome these limitations, thereby creating a functional PEGDA-PCL scaffold. This study examined the physical, mechanical, and biological properties of the PEGDA and PEGDA-PCL scaffolds to determine the effect of PCL coating on PEGDA. The physical characterization of PEGDA-PCL samples demonstrated the effectiveness of combining PCL with PEGDA scaffold to expand its applications in tissue engineering. This study also found a significant improvement of elasticity of PEGDA due to the addition of PCL layers. This study shows that PEGDA-PCL scaffold provides an ideal environment that supports soaks simulated body fluid with time. In addition, cell viability tests shows that the cell adhere, proliferated, and migrated in the PEGDA-PCL scaffold. Therefore, PCL ENF coating has positive influence on PEGDA scaffold.

#### 5.2 Background and Significance

Tissue engineering (TE) holds great promise for the cultivation of patient-specific tissues for restoring organ functions and/or curing various diseases [1-3]. TE techniques involve seeding or implantation of cells into scaffolds which are biodegradable and capable of supporting three-dimensional (3D) cell growth. Photosensitive hydrogels, such as Polyethylene Glycol Diacrylate (PEGDA) are an important class of biomaterials with many TE applications [7-9].

Photolithography is a commonly used process in micro-fabrication to produce the desired scaffold with specific shape and size using a mold [10]. The ability to control the porosity of photosensitive hydrogel such as Polyethylene Glycol Diacrylate (PEGDA) to elicit altered cell

behaviors, including cell adhesion, has raised heightened interest in the scaffold materials for various biomedical applications such as orthopedic repair and regeneration [11] and liver tissue engineering [12]. We have used PEGDA to generate 3D scaffolds in our research [58]. Several PEGDA hydrogel scaffolds have been developed for the reconstruction of injured hard and soft tissues, although the *in vivo* performances have not reported yet [59, 60]. The reason for using PEGDA in our research over other materials is that a thin layer of PEGDA membrane can be manufactured readily to allow for cell growth. In addition, any custom shape membrane can be fabricated using PEGDA using a 3D printed mold.

PEGDA scaffolds having thickness higher than 1 mm were shown to have limited applications as a three-dimensional cell culture device due to the inability of cells to survive within the scaffolds [60]. Cells that are placed deep inside the PEGDA scaffold with a thickness higher than 1 mm die out due to the lack of having access to adequate nutrients. Lack of porosity in the PEGDA scaffold leads the cells to non-uniform tissue regeneration. PEGDA scaffolds need to be designed with intricate architecture, porosity, pore size and shape, and interconnectivity in order to provide the required structural strength, nutrient transport, and micro-environment for cell and tissue in-growth. There is a significant need for scientific research to investigate methods that can overcome the limitations exhibited by thick PEGDA for TE applications. Various PEGDA-based scaffolds were researched, however none of them fulfill all the requirements for TE applications [15, 61, 62]. Overcoming the functional deficits of PEGDA for TE applications motivates this research.

Electrospinning is a process by which fibers with micro to nanometer diameters can be fabricated from an electrostatically driven jet of polymer solution. These fibers have a high surface area to volume ratio, which can have numerous industrial applications as barrier fabrics, wipes, medical, and pharmaceutical uses. In our early research, we have developed electrospin process to produce polycaprolactone (PCL) electrospun nanofiber (ENF) membrane that has competing performances as a functional coating material. The thickness of our PCL ENF membrane is usually in the range of micron. In other research efforts, researchers have reported that the biological functions of ENF membrane depend upon the fiber material, fiber size, and thickness of the membrane [7]. There is no research to date conducted to determine the influence of ENF membrane on the mechanical and biological performances of the PEGDA scaffold. There is still a significant need for scientific research to overcome physical (porosity, water

absorption), mechanical (stiffness, elasticity) and biological (cell adherence, proliferation, and migration) limitations of thick PEDGA hydrogel membranes for tissue engineering applications [63]. Therefore, the goal of this study focuses on the physical, mechanical and biological capabilities of PEDGA-PCL scaffold and evaluate the capabilities for tissue engineering applications.

### 5.3 Materials and methods

#### 5.3.1 Materials

Two solutions were combined to make the PEGDA hydrogel solution mix. The first solution consisted of the liquid Polyethylene Glycol Diacrylate (PEGDA),  $M_n = 700$  (mol), diluted with liquid Dulbecco's Phosphate Buffer Saline (PBS). The second solution consisted of a solute solid photo-initiator (PI) Alpha-alpha-dimethoxy-alpha-phenylacetophenone,  $M_w = 256.35$  (g/mol); Sigma-Aldrich, that was dissolved in the liquid solvent 1-vinyl-2-pyrrolidone,  $M_w = 111.14$  (g/mol). PCL beads (pellet size~3 mm, average  $M_n$  80,000) and acetone (laboratory reagent  $\geq 99.5\%$ ) were sonicated for 30 minutes to prepare the PCL solution.

#### 5.3.2 Sample preparation

##### 5.3.2.1 Sample design

This study prepared two groups of cylindrical specimens: PEGDA and PEGDA-PCL. The specimen dimension closely depends on of the silicone mold which is 10 mm and 1.5 mm thickness. Each group of samples was prepared for six different experiments: SEM images of the surface and histological longitudinal section, DMEM absorption, compression, rheological, and cell viability tests.

##### 5.3.2.2 Sample fabrication process

The researchers in this study fabricated an electrospinning-UV polymerization system. The details of working principle of the system have been recently presented by Abuabed *et al.* [64]. The system can produce any dimension of cylindrical shape PEGDA-PCL scaffold. Specifically, this study fabricated 10 mm diameter and 1.5 mm thickness PEGDA-PCL scaffold. This

dimension is selected due to the suitability of cell culturing for biocompatibility tests on each group of samples in 48 well plate.

**Error! Reference source not found.** illustrates functional elements of a notional combined ENF production-UV photopolymerization unit for automatic production of the 3D scaffold. The notional system combines an ENF production unit and UV polymerization unit and a robotic arm for fiber harvesting. Using a system with these functional elements, any number of PCL ENF and PEGDA membranes may be produced in any shape of 3D scaffolds.

A substrate may be adapted to produce a 3D scaffold comprising at least two equal linear dimensions, or a circular shape. In this study, we have used circular shape collector as shown in **Figure 5-2**: (a) An integrated electrospun-UV photo polymerization-machine; (b) Twelve layers of aligned PCL ENF deposited on the acrylic mold; fabricated samples (c) PEGDA and (d) PEGDA-PCL.

a. PCL pellets (7.69 wt%) were mixed with acetone in an ultrasonic mixer (Sonics & Materials, Inc., model # Vibra-cell VCX 130). The sonication process was carried out at approximately 60°C for 30 minutes. A syringe pump (**Error! Reference source not found.-1A**) is used to feed PCL solution into glass syringe (Fig 5-1B) and flow through a tube (Fig 5-1C) to a metallic needle (**Error! Reference source not found.D**). The metallic disc collectors (**Error! Reference source not found.E**) are spun using speed controlled, direct current (DC) motors. The syringe needle (**Error! Reference source not found.D**) is electrically excited by applying a high-voltage (15 KVA) (**Error! Reference source not found.F**) produced by the power supply. This electrically charged syringe needle for electrospinning synthetic polymer fiber streams is positioned above and substantially centered between the edges of metallic collectors. This will realize an electrical potential difference between the needle tip and the disks, the positioning being adjustable by Z position control stage (**Error! Reference source not found.G**). As a result, an electrostatic field is formed between the charged syringe needle and the edges of the rotating metallic disks. This enables capturing, depositing and aligning fiber between the rotating parallel collectors. A 25 x 25 x 25 mm square block with 10 mm diameter through hole is used to collect fiber. A “smart” robotic arm (**Error! Reference source not found.J**) in a track (**Error! Reference source not found.K**) is used to collect the twelve layers of aligned fibers from the parallel collector on the top of the acrylic substrate. A hollow silicone mold (inner diameter 10 mm and thickness 5 mm) is placed on top of an acrylic substrate such that the hole of the silicone

mold aligned with the hole of the acrylic. The acrylic substrate feed it to the curing station without manually intervening in this process.

The photoinitiator (Alpha-alpha-dimethoxy-alpha-phenylacetophenone) was mixed with solvent (1-vinyl-2-pyrrolidone) to prepare photoinitiator mixture. PEGDA was mixed with PBS to prepare PEGDA mixture. The PEGDA and photoinitiator mixtures were mixed in the desired amount to prepare 0.2% and 0.6% of photoinitiator PEGDA. A second syringe pump system (Error! Reference source not found.L) with spray/needle tip (Error! Reference source not found.M) is used to deposit PEGDA solution on the top of fiber matrix. The silicone mold (Error! Reference source not found.N) is used to cure 1.5 mm thick PEGDA layer on the top of fiber matrix using a UV light (Error! Reference source not found.O).

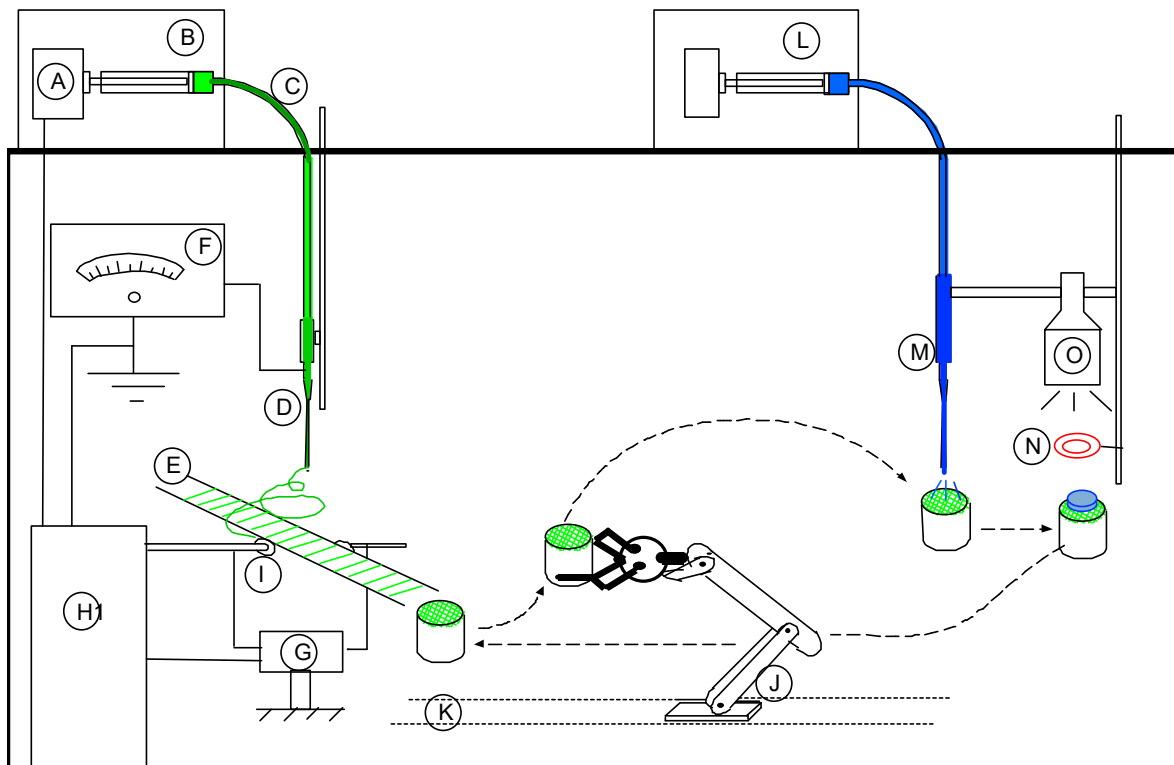


Figure 5-1: Schematic representation of a PEGDA-PCL scaffold [65]. The process b-c-d can be repeated multiple times to create higher thickness scaffold.

### 5.3.3 Experiments

#### 5.3.3.1. SEM and histological examination

To observe the fiber embedding in PEGDA, the fiber layer surface of PEGDA-PCL scaffold was viewed under Hitachi TM 3000 SEM. For PEGDA samples, SEM image was captured on



the flat surface of PEGDA. To view the internal architecture of PEGDA and PEGDA-PCL scaffold, both groups of samples were embedded in paraffin. The paraffin embedded samples were cut longitudinally using a microtome. Multiple longitudinal micro sections were produced for SEM imaging.

#### 5.3.3.2. Mechanical tests

Each group of samples was mounted between the holders in Evex mechanical test equipment. The sample was compressed to 80% of the gel height at a rate of 0.001 mm/sec during the unconfined compression tests. The load and the corresponding displacement of the scaffolds were directly recorded from EVEX machine software. The slopes of the curves were utilized to compare the difference in stiffness between the samples. Oscillation tests were performed on both group of samples using the Malvern CVO-100 rheometer at 5% strain rate at frequency 1 Hz. Viscous, elastic and complex modulus was found from the experiment.

#### 5.3.3.3 Bioactivity

##### *A. Absorption test*

The *in vitro* bioactivity of the scaffolds was assessed by soaking each group of scaffolds in DMEM for 7, 14, and 21 days, respectively. The initial weight of the scaffold,  $W_0$  was measured. After each time period, the weight of the scaffold was measured,  $W_t$ . The value of the rate of DMEM absorption in percentage was measured using the formula:  $(W_t - W_0) \times 100\% / W_0$ .

##### *B. Cell Cultures*

The cells used in this study were cultured and maintained as described in our previous published work [66]. Briefly, Human hepatocellular carcinoma cells (GS5 cells) were cultured in Dulbecco's modified Eagle's medium (DMEM) supplemented with 1x Pen/Strep, 1x non-essential amino acids and 10% fetal bovine serum, and maintained at 37°C and 5% CO<sub>2</sub>. Cells maintained at 80% confluency were used for all our experiments in this study.

##### *C. Cell Viability Assay*

We evaluated the biocompatibility of our PEGDA-PCL scaffold using GS5 cells. We used alamarBlue® to determine the GS5 cell viability on our scaffold at 7 days and 14 days using the

protocol described in our previous work [67]. All samples were tested in triplicates, scaffolds soaked in media without cells served as a control for our experiments. The data was reported as a mean  $\pm$  standard deviation. PEGDA- PCL scaffolds were sterilized using ultraviolet for 30 min. GS5 cells at a concentration of  $1 \times 10^5$  cells per 50  $\mu$ l were seeded onto the scaffold and incubated for 1 hr. The scaffolds were then transferred to 12 well plate and cultured in DMEM medium as described above. The plates were incubated for 7 and 14 days and cell culture media was replaced every 3 days. After an incubation period (7 or 14 days) alamarBlue® was added at a concentration of 100  $\mu$ l per ml and incubated for additional 8 hours. Contents of each well were mixed using a pipettor, 200  $\mu$ l were transferred to a 96-well plate and absorbance was determined by a spectrophotometer at 570nm using 600nm as a reference wavelength. The total number of viable cells attached to the scaffold was calculated using a standard curve which was generated by aliquoting cells into a 96-well plate within the range of 50,000–2,000,000 cells/well. A standard curve was generated by plotting number of cells versus absorbance.

#### *D. Microscopy and Staining*

Attachment of GS5 cells to PCL nanofiber, their ability to migrate into PEGDA scaffold were determined using microscopy and H&E staining techniques. After 7 and 14 days of incubation, the control and test scaffolds were directly imaged using Leica light microscope with imaging software at 200X total magnification. For H&E staining, Scaffolds were transferred into a fresh 12 well plate and rinsed twice with 4.5 ml of PBS to get rid of any nutrient media. Scaffolds were then fixed in 4.5ml of formalin solution for 4 hours at room temperature. After incubation, scaffolds were rinsed twice with 70% ethanol and left in ethanol for 30 mins. Then they were dehydrated using 80, 90 and 100% ethanol with 30 min incubation at room temperature. Scaffold samples were paraffin embedded, sectioned (10-15  $\mu$ m) and stained by Precision Histology Labs Inc (Oklahoma City, OK). Stained slides were examined and imaged using Leica light microscope at 400X total magnification.

## 5.4 Results

### 5.4.1 Fabrication of an electrospin unit for the production of PEGDA scaffold

For the purpose of conducting this study, the researchers have designed and fabricated an integrated electrospun-UV photo polymerization-machine (Figure 5-2: (a) An integrated electrospun-UV photo polymerization-machine; (b) Twelve layers of aligned PCL ENF deposited on the acrylic mold; fabricated samples (c) PEGDA and (d) PEGDA-PCL.

2a) to produce PEGDA-PCL scaffold. The machine utilizes a patented dual disk based mechanism to collect the nanofiber [52]. A robotic arm was developed to automate the machine and reduce the human interference with the machine. The machine is capable of producing twelve layers of aligned uni-direction fibers on an acrylic mold (Figure 5-2: (a) An integrated electrospun-UV photo polymerization-machine; (b) Twelve layers of aligned PCL ENF deposited on the acrylic mold; fabricated samples (c) PEGDA and (d) PEGDA-PCL.

5-2b). The UV photo polymerization unit is used to produce the 1.5 mm thickness and 10 mm diameter PEGDA scaffold (Figure 5-2: (a) An integrated electrospun-UV photo polymerization-machine; (b) Twelve layers of aligned PCL ENF deposited on the acrylic mold; fabricated samples (c) PEGDA and (d) PEGDA-PCL.

c). Both electrospun and UV photo polymerization units are simultaneously used to produce PEGDA-PCL scaffold where the bottom and top surface of the PEGDA was covered by twelve layers of aligned PCL ENF (Figure 5-2: (a) An integrated electrospun-UV photo polymerization-machine; (b) Twelve layers of aligned PCL ENF deposited on the acrylic mold; fabricated samples (c) PEGDA and (d) PEGDA-PCL.

d). Non-uniform surface topography and voids were observed on PEGDA samples (Figure 5-2: (a) An integrated electrospun-UV photo polymerization-machine; (b) Twelve layers of aligned PCL ENF deposited on the acrylic mold; fabricated samples (c) PEGDA and (d) PEGDA-PCL.

c), where PEGDA-PCL samples were characterized by uniform surface architecture (Figure 5-2: (a) An integrated electrospun-UV photo polymerization-machine; (b) Twelve layers of aligned PCL ENF deposited on the acrylic mold; fabricated samples (c) PEGDA and (d) PEGDA-PCL.

d) due to the coating of PCL ENF.

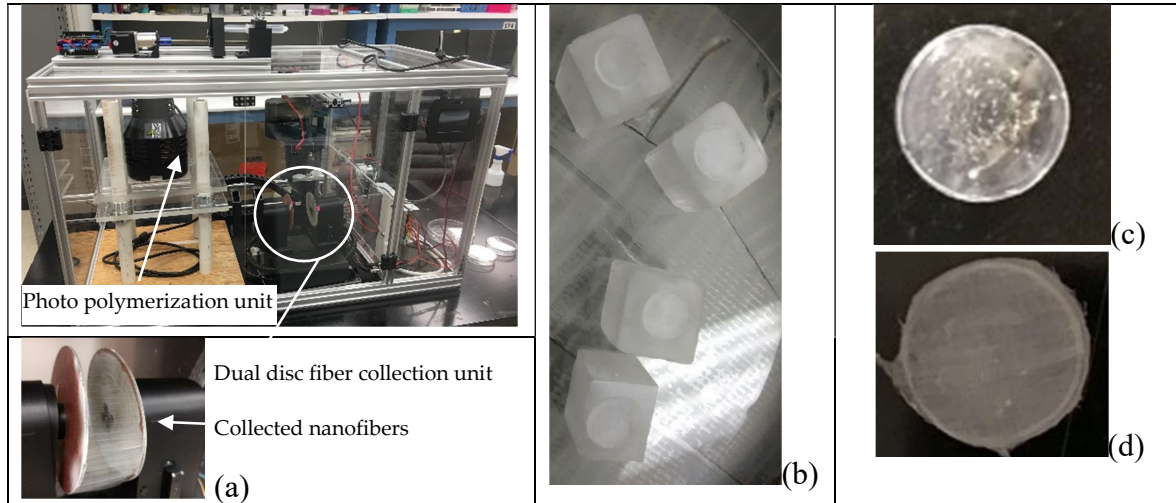


Figure 5-2: (a) An integrated electrospun-UV photo polymerization-machine; (b) Twelve layers of aligned PCL ENF deposited on the acrylic mold; fabricated samples (c) PEGDA and (d) PEGDA-PCL.

#### 5.4.2 Surface characterization

We have compared the SEM images of a fiber layered surface and sectioned image of the PEGDA and PEGDA-PCL scaffold. A higher surface artifacts of PEGDA-PCL scaffold due to PCL ENF arrangement (Figure 5-3: SEM images of top surface of (a) PEGDA and (b) PEGDA-PCL scaffolds. PCL-PEGDA samples shows higher amount of artifacts in compare to PEGDA. SEM images of paraffin embedded and sectioned scaffolds: (c) PEGDA and (d) PCL-PEGDA. Red arrows in Figure 4d shows the presence of PCL ENF in PEGDA.

a) was observed when compared to PEGDA scaffold (Figure 5-3: SEM images of top surface of (a) PEGDA and (b) PEGDA-PCL scaffolds. PCL-PEGDA samples shows higher amount of artifacts in compare to PEGDA. SEM images of paraffin embedded and sectioned scaffolds: (c) PEGDA and (d) PCL-PEGDA. Red arrows in Figure 4d shows the presence of PCL ENF in PEGDA.

b). The sectioned images of paraffin-embedded PEGDA (Figure 5-3: SEM images of top surface of (a) PEGDA and (b) PEGDA-PCL scaffolds. PCL-PEGDA samples shows higher amount of artifacts in compare to PEGDA. SEM images of paraffin embedded and sectioned scaffolds: (c) PEGDA and (d) PCL-PEGDA. Red arrows in Figure 4d shows the presence of PCL ENF in PEGDA.

c) and PEGDA-PCL (Figure 5-3: SEM images of top surface of (a) PEGDA and (b) PEGDA-PCL scaffolds. PCL-PEGDA samples shows higher amount of artifacts in compare to PEGDA. SEM images of

paraffin embedded and sectioned scaffolds: (c) PEGDA and (d) PCL-PEGDA. Red arrows in Figure 4d shows the presence of PCL ENF in PEGDA.

d) scaffold shows the porosity of both scaffolds. The engrossed PCL ENF layers in PEGDA scaffold can be seen from the PEGDA-PCL scaffold.

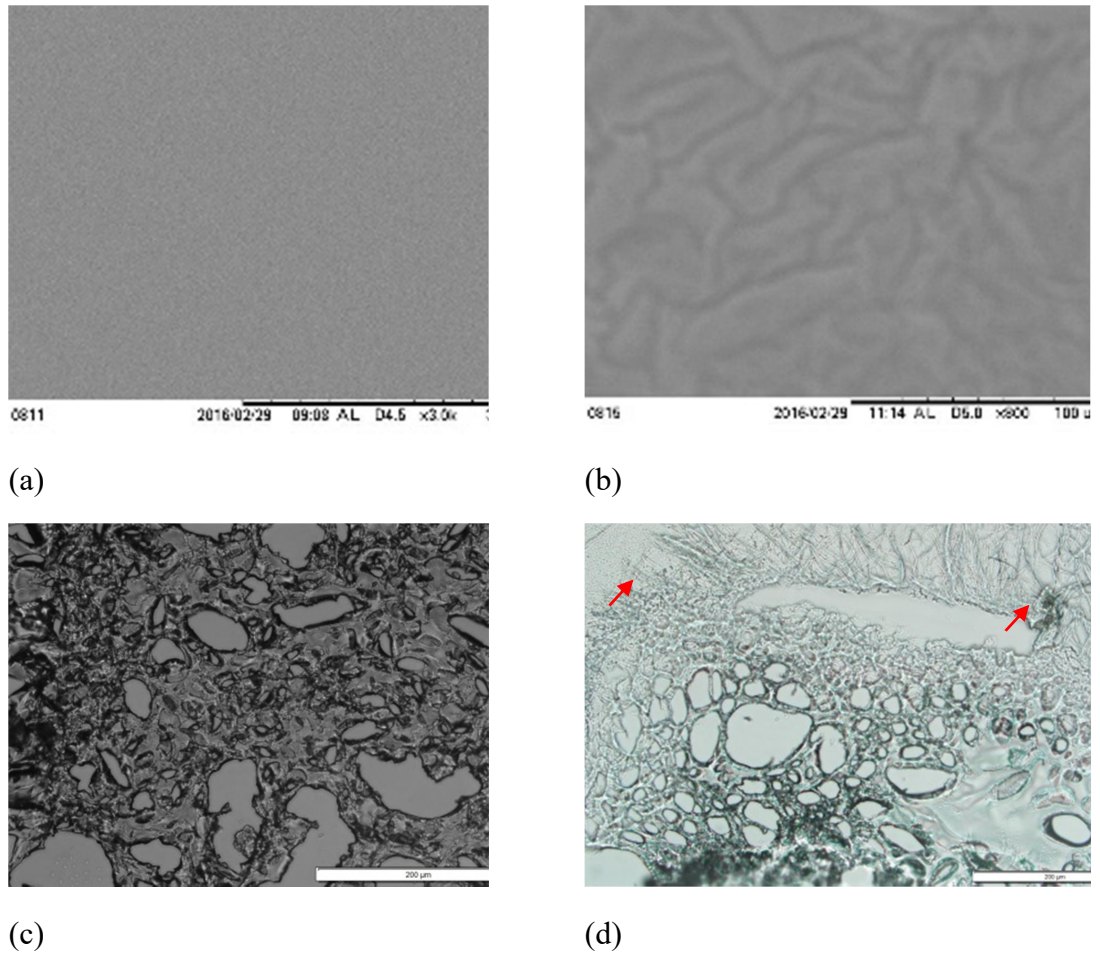


Figure 5-3: SEM images of top surface of (a) PEGDA and (b) PEGDA-PCL scaffolds. PCL-PEGDA samples shows higher amount of artifacts in compare to PEGDA. SEM images of paraffin embedded and sectioned scaffolds: (c) PEGDA and (d) PCL-PEGDA. Red arrows in Figure 4d shows the presence of PCL ENF in PEGDA.

#### 5.4.3 Mechanical tests

There is a significant difference in mechanical properties between PEGDA and PCL-PEGDA scaffolds during the unconfined compression tests ( $p < 0.05$ ). **Error! Reference source not found.**-4 shows that PEGDA-PCL composite scaffold can absorb a higher amount of

compressive stress compared to PEGDA under a loaded condition (>10 N). The average compressive stiffness and modulus of PEGDA-PCL scaffold were higher than that of PEGDA (**Error! Reference source not found.**). The results confirmed that PCL ENF membrane can reinforce the PEGDA scaffold.

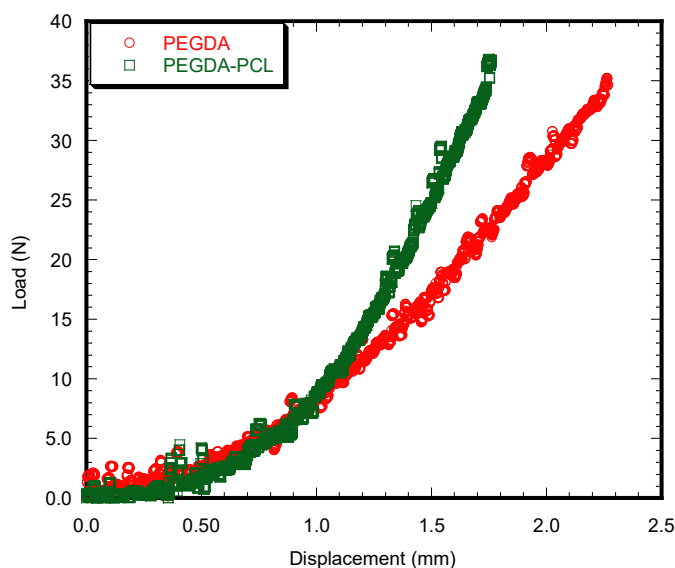


Figure 5-4: Load vs. displacement plot of a PEGDA and PEGDA-PCL scaffold under static compression loading.

Experimental parameters	PEGDA	PEGDA-PCL
Compressive stiffness (N/mm)	3.00± 0.12	5.36 ± 0.02*
Compressive modulus (kPa)	259.68 ± 3.56	509.61± 0.01*

Table 5-1: Difference between mechanical properties between PEGDA and PEGDA-PCL scaffolds during compression. Both samples have same diameters (10 mm) and loaded up to 35 N to calculate the mechanical properties. Data presented n=3 for both samples. Data presented as a mean ± standard error. Note: \*p<0.05 (compared to PEGDA).

This study reported a significant difference of viscoelastic behavior between PEGDA and PCL-PEGDA scaffolds during the rheological tests ( $p<0.05$ ). As like as the compression test, the rheological tests show that PEGDA-PCL composite scaffold can absorb a higher amount of shear stress compared to PEGDA due to the increase of shear strain (Figure 5-5: Rheological tests were performed on the hydrogel using the Malvern CVO-100 rheometer at 5% strain rate at frequency 1 Hz. (a) shear stress vs. strain and (b) complex modulus with respect to time was found from the experiment.

a). The average resultant shear modulus (referred as complex modulus) of PEGDA-PCL scaffold was higher than that of PEGDA (Figure 5-5: Rheological tests were performed on the hydrogel using the Malvern CVO-100 rheometer at 5% strain rate at frequency 1 Hz. (a) shear stress vs. strain and (b) complex modulus with respect to time was found from the experiment.

b). The enormous difference of phase angle between PEGDA and PEGDA-PCL confirms that PCL ENF membrane has a strong influence on the viscoelastic characteristics of PEGDA. This happens due to the fact that the attachment of PCL fiber layers with PEGDA increases elastic modulus, but decreases the viscous modulus (**Error! Reference source not found.**).

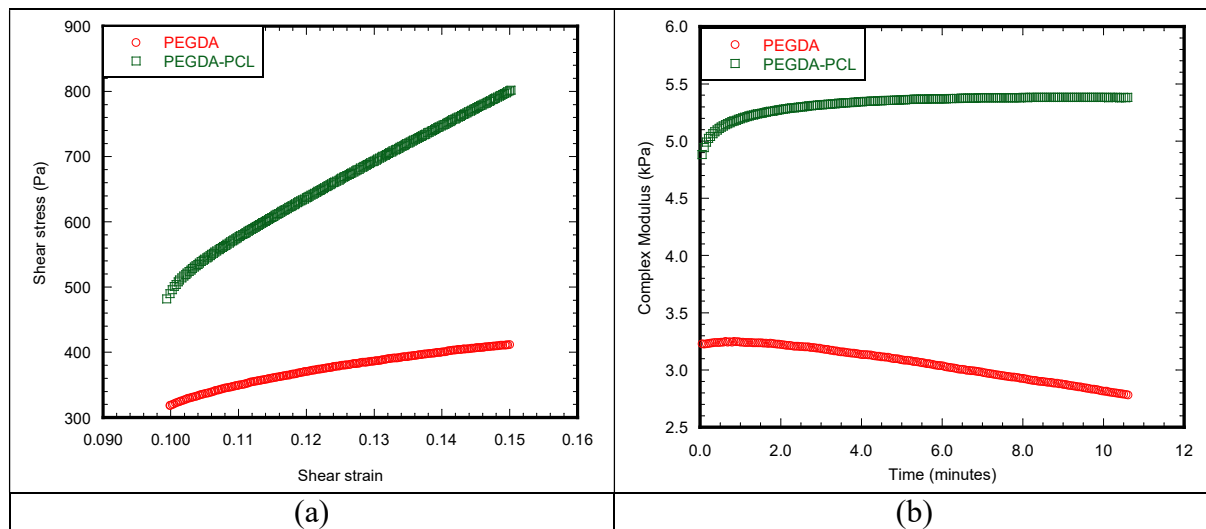


Figure 5-5: Rheological tests were performed on the hydrogel using the Malvern CVO-100 rheometer at 5% strain rate at frequency 1 Hz. (a) shear stress vs. strain and (b) complex modulus with respect to time was found from the experiment.

Experimental parameters	PEGDA only	PEGDA-PCL
Viscous modulus (kPa)	1.01± 0.24	0.53± 0.18*
Elastic modulus (kPa)	2.82± 0.12	5.34 ± 0.23*
Phase shift angle (degree)	19.72± 0.40	5.68± 0.22*

Table 5-4-2: Difference between viscoelastic properties between PEGDA and PCL-PEGDA scaffolds. Both samples have same diameters (9.56 mm). Data presented n=3 for both samples. Data presented as mean ± standard error. Note: \*p<0.05 (compared to control).

#### 5.4.4 Bioactivity

Bioactivity of the scaffolds was assessed by soaking in simulated body fluid (DMEM) for 7, 14, and 21 days. Both PEGDA and PEGDA-PCL samples show the capability of absorption of DMEM with time (**Error! Reference source not found.**). Though the rate of absorption of

DMEM was found higher for the first week in compare to PEGDA-PCL ( $p < 0.5$ ), but there is no significant difference in absorption rate after the second and third week during the absorption tests between the samples. This means fiber does not have any effect on the absorption of DMEM after 1 week of soaking the sample in the media.

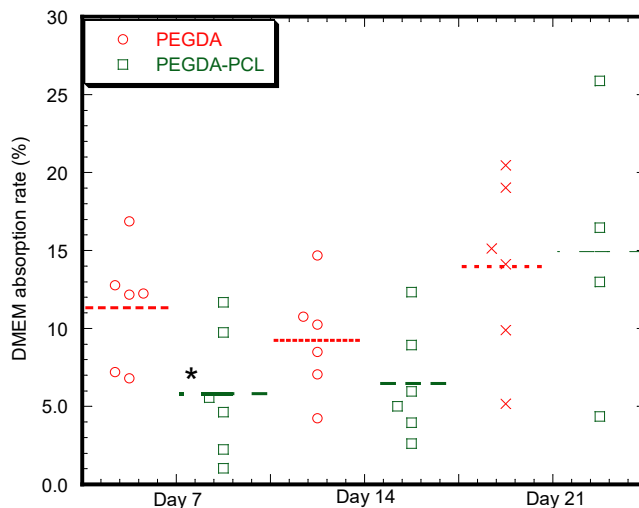


Figure 5-6: DMEM absorption rate with respect time. Note: \* $p < 0.05$  (compared to PEGDA).

Liver-derived hepatoma cells (GS5 cells) were used to test cytocompatibility of our composite scaffolds after 7 and 14 days of incubation. **Error! Reference source not found.** (BF) show light microscope image of hepatocytes attached to PCL nanofiber. The cells are holding onto PCL material using cytoplasmic extensions (**Error! Reference source not found.** BF and CF) and more attachment can be seen at the PCL junctions. These cells still retain their hepatocyte morphology with an average size of 5-10  $\mu\text{m}$ . As the cells proliferate they form spheroid like structures attached to PCL fibers. Fig 5-7 (BS and CS) show cell that have migrated into PEGDA hydrogel and formed spheroids. Spheroids appear to be progressing into PEGDA scaffold. Morphology of hepatocytes in our PEGDA-PCL scaffold closely resemble functional spheroids reported elsewhere [12, 68] forming multi-cellular aggregates. The increase in spheroid size between 7 and 14 days shows that nutrients and oxygen are able to percolate through the material and support cell growth.



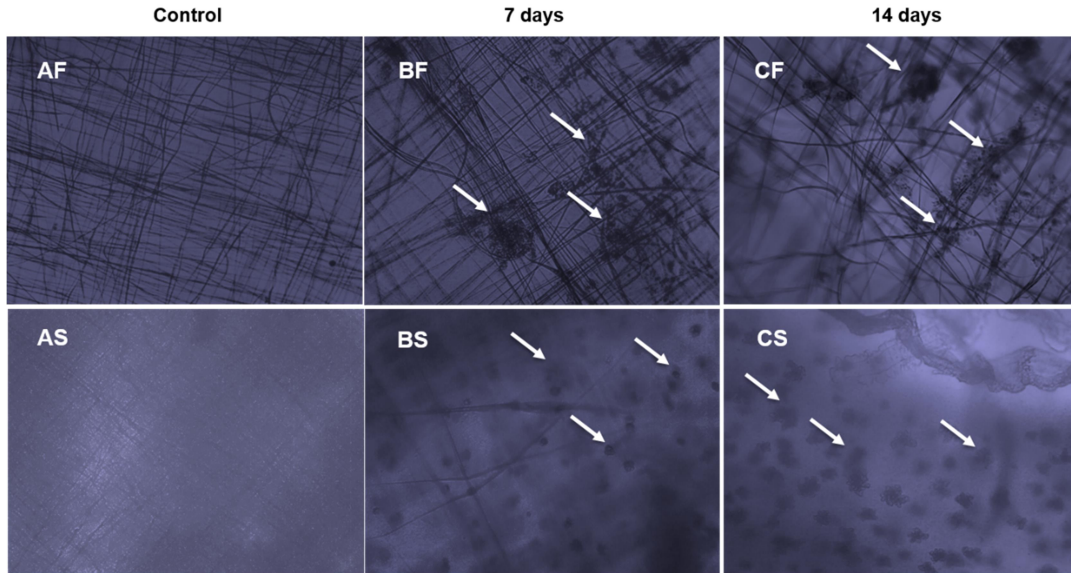


Figure 5-7: GS5 cells attached to 12 layers of PCL nanofiber (Panel BF and CF) sandwiching the PEGDA scaffold. Panel BS and CS represent cells growing embedded in PEGDA. Panel AF and AS are control scaffold without cells. White arrows point to cells. All scaffolds were incubated for 7 and 14 days. Images were taken using Leica light microscope at 100X total magnification.

Our H&E staining results (**Error! Reference source not found.**) also corroborate this observation. It shows that cells have migrated from the top ( the area where the fibers were deposited) and moved towards the other side of the scaffold.

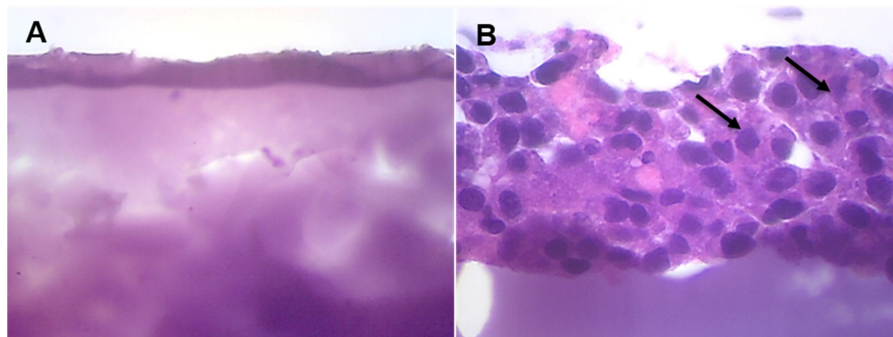


Figure 5-8: H&E staining of PEGDA-PCL scaffolds with GS5 cells (Panel B) after 7 days. Black arrows in panel B point to cells. Panel A is control scaffold without any cells. Leica light microscope at 400X magnification.

Cell viability was measured using alamarBlue® with results shown in Figure 5-9. Our results clearly indicate that cells are viable at 7 and 14 days and proliferating. During the first

week of incubation, there is a significant increase in cell number ( $p < 0.0001$ ). During the second week of incubation, the cells continued to proliferate with an 8.1% increase in cell number.

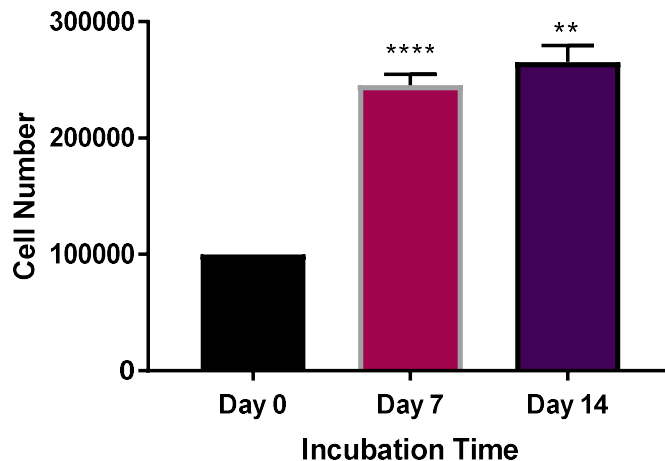


Figure 5-9: Increase in cell number on PEGDA-PCL scaffold with time. GS5 cell Viability after 7 and 14 days on PCL-PEGDA scaffolds using alamarBlue® assay. Our results clearly indicate that cells remain viable on our scaffolds. Values are mean  $\pm$  SD of triplicates.

## 5.5 Discussion

This study has successfully fabricated electrospun-UV polymerization systems that can produce 10 mm diameter and 1.5 mm thickness PEGDA-PCL scaffold. This machine is capable of assembling PCL and PEGDA membranes simultaneously in layers to produce larger thickness and custom shape PEGDA-PCL scaffold. Such scaffold can meet the mechanical and biological requirements for successful integration with human body which is the future direction of this research.

We have observed increased amount of DMEM absorption capabilities with time for both PEGDA and PEGDA-PCL samples due to the porosity of both samples. The volume of the voids expands with time due to degradation, which increases the DMEM absorption rate. There was no significant difference in DMEM absorption capabilities between PEGDA and PEGDA-PCL after 1 week of the DMEM absorption test.

Results showed that our developed scaffolds satisfied the minimum compressive modulus requirement for bone graft substitutes ( $>0.5\text{MPa}$  [69]). Further improvement of stiffness and other mechanical properties of PEGDA scaffold is possible by optimizing the porosity of PCL

ENF membrane and immobilization of osteoconductive nanoparticles such as hydroxyapatite, MgO with PCL nanofiber in the scaffold. The other way is to increase the number of layers of PCL and PEGDA membranes. PCL membranes provide interconnectivity between two PEGDA membrane layers. It can serve as an entrapment device to provide the required structural strength, nutrient transport, and micro-environment for cell and tissue in-growth to the adjacent PEGDA layers.

A 3D scaffold provides a 3D environment in which cells are better able to mimic their in vivo counterparts. Our results clearly demonstrate that twelve layers of PCL nanofiber on 1.5 mm thick PEGDA provides an ideal surface area for cell attachment, allowing transfer of nutrients, oxygen and removal of metabolic waste from cell growth sites. PCL nanofiber provides an ideal surface for cells to spread well and attach firmly (**Error! Reference source not found.**). Considering the results from cell viability and staining (**Error! Reference source not found.**), we are convinced that our composite scaffold is ideal for cell response and adhesion.

The variability of the physical and mechanical characteristics in this study was due to the difference of the ENF and PEGDA membrane thickness and architectures in PEGDA-PCL scaffolds. It is impossible to collect the same ENF architecture from the harvested aligned unidirectional ENFs using the dual disc collector. There is variability in hydrogel membrane thickness and architectures in PEGDA and PEGDA-PCL scaffolds since it is impossible to deposit the same amount of hydrogel and cure under same conditions using the photo-polymerization curing systems. These limitations can be overcome by fine tuning the integrated UV photo-polymerization system as well as testing a large number of samples.

The study revealed that PEGDA-PCL scaffold provides a fundamental aspect for producing a tissue scaffold with better mechanical and biological capabilities than a scaffold comprised with PEGDA only. A literature search has revealed no reported research directed to PEGDA-PCL scaffold in relation to the influence of PCL ENF coating on the physical, mechanical and biological performances of a composite scaffold. Therefore, we are unable to verify our results with others. Shanjani *et al.* [70] fabricated and characterized well-defined porous PCL- beta-tricalcium phosphate scaffolds with identical pore size (500 $\mu$ m) but different strut sizes (200 and 400 $\mu$ m) using additive manufacturing technology and filled the porous scaffold by PEGDA hydrogel. In our research, the PEGDA and PCL membranes can be stacked and interspersed

between multiple layers of PCL membranes, binding them together to produce a three-dimensional (3D) composite scaffold. Our patent pending approach [65] is significantly different than the approach used by the previous researchers. Studies investigating the influence PCL ENF has on PEGDA- PCL scaffolds are required for the design of PEGDA- PCL scaffolds that produce better clinical outcomes for tissue engineering applications.

## 5.6 Conclusions

This study shows a method for the incremental advancement and translation of PCL ENF to produce a functional PEGDA based scaffold for tissue engineering. The feasibility of depositing multiple layers of PCL ENF on PEGDA was explored. This study shows that the mechanical and biological performances of PEGDA scaffold can be significantly improved by using highly organized and high porosity electrospun nanofiber matrix. This study will lead to the production of a novel PEGDA-PCL composite scaffold that may have competing performances with the commercially available scaffolds for biomedical applications.

## References

- [1] Fett, T., 1999, "Stress intensity factors for edge-cracked plates under arbitrary loading," *Fatigue & Fracture of Engineering Materials & Structures*, **22**(4), pp. 301-305.
- [2] Brunette, D.M., Tengvall, P., Textor, M., and Thomsen, P., 2001, *Titanium in medicine: Material science, surface science, engineering, biological responses and medical applications*, 1 ed.
- [3] Lennon, A.B., McCormack, B.A.O., and Prendergast, P.J., 2003, "The relationship between cement fatigue damage and implant surface finish in proximal femoral prostheses," *Medical Engineering and Physics*, **25**(Compendex), pp. 833-841.
- [4] Lee, S.C., Hwang, B.W., Lee, S.J., Choi, H.Y., Kim, S.Y., Jung, S.Y., Ragupathy, D., Lee, D.D., and Kim, J.C., 2011, "A novel tin oxide-based recoverable thick film so<sub>2</sub> gas sensor promoted with magnesium and vanadium oxides," *Sensors and Actuators B: Chemical*, **160**(1), pp. 1328-1334.
- [5] Mardare, D., Cornei, N., Mita, C., Florea, D., Stancu, A., Tiron, V., Manole, A., and Adomnitei, C., 2016, "Low temperature tio<sub>2</sub> based gas sensors for co<sub>2</sub>," *Ceramics International*, **42**(6), pp. 7353-7359.
- [6] Kumar, R., Al-Dossary, O., Kumar, G., and Umar, A., 2015, "Zinc oxide nanostructures for no<sub>2</sub> gas-sensor applications: A review," *Nano-Micro Letters*, **7**(2), pp. 97-120.
- [7] Bosworth, L.A., Turner, L.-A., and Cartmell, S.H., 2013, "State of the art composites comprising electrospun fibres coupled with hydrogels: A review," *Nanomedicine: Nanotechnology, Biology and Medicine*, **9**(3), pp. 322-335.
- [8] Varghese, S., and Elisseeff, J.H., "Hydrogels for musculoskeletal tissue engineering," in *Polymers for regenerative medicine, Advances in polymer science*, pp. 95-144, 2006.
- [9] Xin, A.X., Gaydos, C., and Mao, J.J., 2006, "In vitro degradation behavior of photopolymerized peg hydrogels as tissue engineering scaffold," *Conference proceedings : ... Annual International Conference of the IEEE Engineering in Medicine and Biology Society. IEEE Engineering in Medicine and Biology Society. Annual Conference*, **1**, pp. 2091-3.
- [10] Yasar, O., Orock, A., Tarantini, S., White, J., and Khandaker, M., "Mechanical characterization of polyethylene glycol diacrylate (pegda) for tissue engineering applications," in *Mechanics of biological systems and materials, volume 5, Conference proceedings of the society for experimental mechanics series*, B. C. Prorok, F. Barthelat, C. S. Korach, K. J. Grande-Allen, E. Lipke, G. Lykofatitits, and P. Zavattieri, Eds.: Springer New York, pp. 189-195, 2013.
- [11] Lee, K.Y., and Mooney, D.J., 2001, "Hydrogels for tissue engineering," *Chemical Reviews*, **101**(7), pp. 1869-1879.
- [12] Chen, F., Tian, M., Zhang, D., Wang, J., Wang, Q., Yu, X., Zhang, X., and Wan, C., 2012, "Preparation and characterization of oxidized alginate covalently cross-linked galactosylated chitosan scaffold for liver tissue engineering," *Materials Science and Engineering: C*, **32**(2), pp. 310-320.
- [13] Im, B.J., Lee, S.W., Oh, N., Lee, M.H., Kang, J.H., Leesungbok, R., Lee, S.C., Ahn, S.J., and Park, J.S., 2012, "Texture direction of combined microgrooves and submicroscale topographies of titanium substrata influence adhesion, proliferation, and differentiation in human primary cells," *Archives of Oral Biology*(0).

- [14] Lamers, E., Frank Walboomers, X., Domanski, M., te Riet, J., van Delft, F.C.M.J.M., Luttge, R., Winnubst, L.A.J.A., Gardeniers, H.J.G.E., and Jansen, J.A., 2010, "The influence of nanoscale grooved substrates on osteoblast behavior and extracellular matrix deposition," *Biomaterials*, **31**(12), pp. 3307-3316.
- [15] Lenhart, S., Meier, M.-B., Meyer, U., Chi, L., and Wiesmann, H.P., 2005, "Osteoblast alignment, elongation and migration on grooved polystyrene surfaces patterned by langmuir–blodgett lithography," *Biomaterials*, **26**(5), pp. 563-570.
- [16] Walboomers, X.F., Monaghan, W., Curtis, A.S.G., and Jansen, J.A., 1999, "Attachment of fibroblasts on smooth and microgrooved polystyrene," *Journal of Biomedical Materials Research*, **46**(2), pp. 212-220.
- [17] Khandaker, M., Riahi-zhad, S., Sultana, F., Vaughan, M., Knight, J., and Morris, T., 2016 "Peen treatment on a titanium implant: Effect of roughness, osteoblast cell functions, and bonding with bone cement.," *International Journal of Nanomedicine*.
- [18] Prodanov, L., te Riet, J., Lamers, E., Domanski, M., Luttge, R., van Loon, J.J.W.A., Jansen, J.A., and Walboomers, X.F., 2010, "The interaction between nanoscale surface features and mechanical loading and its effect on osteoblast-like cells behavior," *Biomaterials*, **31**(30), pp. 7758-7765.
- [19] Ait moussa, A., Fischer, J., Yadav, R., and Khandaker, M., 2017, "Minimizing cement damage and stress shielding of the bone in cemented femoral hip prostheses through computational design optimization," *Advances in Orthopedics*, **2017**.
- [20] Van Lenthe, G.H., de Waal Malefijt, M.C., and Huiskes, R., 1997, "Stress shielding after total knee replacement may cause bone resorption in the distal femur," *The Journal of bone and joint surgery. British volume*, **79**(1), pp. 117-22.
- [21] Gefen, A., 2002, "Optimizing the biomechanical compatibility of orthopedic screws for bone fracture fixation," *Medical Engineering & Physics*, **24**(5), pp. 337-347.
- [22] Haase, K., and Rouhi, G., 2013, "Prediction of stress shielding around an orthopedic screw: Using stress and strain energy density as mechanical stimuli," *Computers in Biology and Medicine*, **43**(11), pp. 1748-1757.
- [23] Eraslan, O., and Inan, O., 2010, "The effect of thread design on stress distribution in a solid screw implant: A 3d finite element analysis," *Clinical oral investigations*, **14**(4), pp. 411-6.
- [24] Faegh, S., and Muftu, S., 2010, "Load transfer along the bone-dental implant interface," *J Biomech*, **43**(9), pp. 1761-70.
- [25] Currey, J.D., 2002, *Bones: Structure and mechanics*, Princeton University Press.
- [26] Biggs, M., Dalby, M., Wilkinson, C., Gadegaard, N., and Richards, G., 2007, "The influence of nanoscale biomimetic structures on osteoblast adhesion," *Comparative Biochemistry and Physiology - Part A: Molecular & Integrative Physiology*, **146**(4, Supplement), pp. S64.
- [27] Travan, A., Marsich, E., Donati, I., Foulc, M.-P., Moritz, N., Aro, H.T., and Paoletti, S., 2012, "Polysaccharide-coated thermosets for orthopedic applications: From material characterization to in vivo tests," *Biomacromolecules*, **13**(5), pp. 1564-1572.
- [28] Zankovych, S., Diefenbeck, M., Bossert, J., Mückley, T., Schrader, C., Schmidt, J., Schubert, H., Bischoff, S., Faucon, M., Finger, U., and Jandt, K.D., 2013, "The effect of polyelectrolyte multilayer coated titanium alloy surfaces on implant anchorage in rats," *Acta Biomaterialia*, **9**(1), pp. 4926-4934.

- [29] Moffat KL, Wang IN, Rodeo SA, and HH., L., 2009 "Orthopedic interface tissue engineering for the biological fixation of soft tissue grafts," *Clin Sports Med.*, **28**(1), pp. 157-76.
- [30] Saha, S., and Pal, S., 1984, "Improvement of mechanical properties of acrylic bone cement by fiber reinforcement," *J Biomech*, **17**(7), pp. 467-78.
- [31] Wagner, H.D., and Cohn, D., 1989, "Use of high-performance polyethylene fibres as a reinforcing phase in poly(methylmethacrylate) bone cement," *Biomaterials*, **10**(2), pp. 139-141.
- [32] Zupančič, Š., Baumgartner, S., Lavrič, Z., Petelin, M., and Kristl, J., 2015, "Local delivery of resveratrol using polycaprolactone nanofibers for treatment of periodontal disease," *Journal of Drug Delivery Science and Technology*, **30**, Part B, pp. 408-416.
- [33] Wu, X., Mahalingam, S., VanOosten, S.K., Wisdom, C., Tamerler, C., and Edirisinghe, M., 2017, "New generation of tunable bioactive shape memory mats integrated with genetically engineered proteins," *Macromolecular bioscience*, **17**(2).
- [34] Wang, H.B., Mullins, M.E., Cregg, J.M., Hurtado, A., Oudega, M., Trombley, M.T., and Gilbert, R.J., 2009, "Creation of highly aligned electrospun poly-l-lactic acid fibers for nerve regeneration applications," *Journal of Neural Engineering*, **6**(1).
- [35] Kwon, I.K., Kidoaki, S., and Matsuda, T., 2005, "Electrospun nano- to microfiber fabrics made of biodegradable copolyesters: Structural characteristics, mechanical properties and cell adhesion potential," *Biomaterials*, **26**(18), pp. 3929-39.
- [36] Po-Yee Lui, P., Zhang, P., Chan, K.-M., and Qin, L., 2010, "Biology and augmentation of tendon-bone insertion repair," *Journal of Orthopaedic Research Surgery and Research*, **5**(59).
- [37] Kim, G.H., 2008, "Electrospun pcl nanofibers with anisotropic mechanical properties as a biomedical scaffold," *Biomedical materials*, **3**(2).
- [38] Khandaker, M., Vaughan, M., Coles, A., Jamadagni, H., Wolf, R., and Williams, W., 2017, "Application of polycaprolactone nanofibers and mgo nanoparticles for a cemented implant surgery," 2017 Orthopaedic Research Society (ORS) Annual Meeting, San Diego, CA.
- [39] Ries, M.D., Rauscher, L.A., Hoskins, S., Lott, D., Richman, J.A., and Lynch, F., 1998, "Intramedullary pressure and pulmonary function during total knee arthroplasty," *Clinical Orthopaedics and Related Research*, **356**, pp. 154-160.
- [40] Graham, J., Ries, M., and Pruitt, L., 2003, "Effect of bone porosity on the mechanical integrity of the bone-cement interface," *Journal of Bone and Joint Surgery-American Volume*, **85A**(10), pp. 1901-1908.
- [41] ASTM, 2006, D790-03: Standard test methods for flexural properties of unreinforced and reinforced plastics and electrical insulating materials, Section 8 ed ASTM International.
- [42] Apedo, K.L., Munzer, C., He, H., Montgomery, P., Serres, N., Fond, C., and Feugeas, F., 2015, "Cement paste surface roughness analysis using coherence scanning interferometry and confocal microscopy," *Materials Characterization*, pp. 108-119.
- [43] Life Technologies Corporation., *Click-it® edu imaging kits* <https://tools.thermofisher.com/content/sfs/manuals/mp10338.pdf>, 2011.
- [44] Khandaker, M., Vaughan, M., Morris, T., White, J., and Meng, Z., 2014, "Effect of additives particles on mechanical, thermal and cell functions properties of poly (methyl methacrylate) cement," *Int J Nanomedicine*.

- [45] Lim, J.Y., Shaughnessy, M.C., Zhou, Z., Noh, H., Vogler, E.A., and Donahue, H.J., 2008, "Surface energy effects on osteoblast spatial growth and mineralization," *Biomaterials*, **29**(12), pp. 1776-1784.
- [46] Ferraz, E.P., Sa, J.C., De Oliveira, P.T., Alves Jr, C., Beloti, M.M., and Rosa, A.L., 2014, "The effect of plasma-nitrided titanium surfaces on osteoblastic cell adhesion, proliferation, and differentiation," *Journal of Biomedical Materials Research - Part A*, **102**(4), pp. 991-998.
- [47] Kumbar, S.G., James, R., Nukavarapu, S.P., and Laurencin, C.T., 2008, "Electrospun nanofiber scaffolds: Engineering soft tissues," *Biomedical materials*, **3**(3).
- [48] Khandaker, M., and Riahinezhad, S., "Method and apparatus to control the heterogeneous flow of bone cement and improve osseointegration of cemented implant." US, 2016.
- [49] Moursi, A.M., Winnard, A.V., Winnard, P.L., Lannutti, J.J., and Seghi, R.R., 2002, "Enhanced osteoblast response to a polymethylmethacrylate-hydroxyapatite composite," *Biomaterials*, **23**(1), pp. 133-44.
- [50] Mahalingam, S., and Edirisinghe, M., 2013, "Forming of polymer nanofibers by a pressurised gyration process," *Macromolecular Rapid Communications*, **34**(14), pp. 1134-1139.
- [51] Deravi, L.F., Sinatra, N.R., Chantre, C.O., Nesmith, A.P., Yuan, H., Deravi, S.K., Goss, J.A., MacQueen, L.A., Badrossamy, M.R., Gonzalez, G.M., Phillips, M.D., and Parker, K.K., 2017, "Design and fabrication of fibrous nanomaterials using pull spinning," *Macromolecular Materials and Engineering*, **302**(3), pp. 1600404-n/a.
- [52] Khandaker, M., and Snow, P., "Method and apparatus for controlled alignment and deposition of branched electrospun fiber," University of Central Oklahoma, US patent application no. US9359694, Int. Patent no. AD01D500FI, 2016.
- [53] Kanungo, I., Fathima, N.N., Rao, J.R., and Nair, B.U., 2013, "Influence of pcl on the material properties of collagen based biocomposites and in vitro evaluation of drug release," *Materials science & engineering. C, Materials for biological applications*, **33**(8), pp. 4651-9.
- [54] Sultanova, Z., Kaleli, G., Kabay, G., and Mutlu, M., 2016, "Controlled release of a hydrophilic drug from coaxially electrospun polycaprolactone nanofibers," *International Journal of Pharmaceutics*, **505**(1-2), pp. 133-138.
- [55] Chong, L.H., Hassan, M.I., and Sultana, N., 2015, "Electrospun polycaprolactone (pcl) and pcl/ nano-hydroxyapatite (pcl/nha)-based nanofibers for bone tissue engineering application," *10th Asian Control Conference (ASCC)*, pp. 1-4.
- [56] Ding, B., Wang, M., Yu, J., and Sun, G., 2009, "Gas sensors based on electrospun nanofibers," *Sensors*, **9**(3), pp. 1609-1624.
- [57] Khandaker, M., Utsaha, K.C., and Morris, T., 2014, "Interfacial fracture toughness of titanium-cement interfaces: Effects of fibers and loading angles," *International Journal of Nanomedicine*, **9**(1).
- [58] Khandaker, M., Oroock, A., Tarantini, S., White, J., and Yasar, O., 2016, "Biomechanical performances of networked polyethylene glycol diacrylate: Effect of photoinitiator concentration, temperature, and incubation time," *International Journal of Biomaterials*, **2016**, pp. 3208312.
- [59] Sun, W., Darling, A., Starly, B., and Nam, J., 2004, "Computer-aided tissue engineering: Overview, scope and challenges," *Biotechnology and Applied Biochemistry*, **39**(1), pp. 29-47.



- [60] Yasar, O., Starly, B., and Lan, S.-F., 2009, "A lindenmayer systems based approach for the design of nutrient delivery networks in tissue constructs," *Journal of Biofabrication*, **1**(4).
- [61] Lee, S.-H., and Shin, H., 2007, "Matrices and scaffolds for delivery of bioactive molecules in bone and cartilage tissue engineering," *Advanced Drug Delivery Reviews*, **59**(4–5), pp. 339-359.
- [62] Bonzani, I.C., Adhikari, R., Houshyar, S., Mayadunne, R., Gunatillake, P., and Stevens, M.M., 2007, "Synthesis of two-component injectable polyurethanes for bone tissue engineering," *Biomaterials*, **28**(3), pp. 423-433.
- [63] Visser, J., Melchels, F.P.W., Jeon, J.E., van Bussel, E.M., Kimpton, L.S., Byrne, H.M., Dhert, W.J.A., Dalton, P.D., Hutmacher, D.W., and Malda, J., 2015, "Reinforcement of hydrogels using three-dimensionally printed microfibrils," *Nat Commun*, **6**.
- [64] Abuabed, A., Rankin, M., Khandaker, M., Forrer, M., Bevel, W., and Varghese, S., 2017, "An automated dual disc electrospun fiber collection method for sensing applications," *The 12th IEEE Sensors Applications Symposium*, Glassboro, New Jersey, USA.
- [65] Khandaker, M., and Riahinezhad, S., "Process and apparatus to create 3d tissue scaffold using electrospun nanofiber matrix and photosensitive hydrogel." US, 2016.
- [66] Rad, A.T., Ali, N., Kotturi, H.S., Yazdimamaghani, M., Smay, J., Vashae, D., and Tayebi, L., 2014, "Conducting scaffolds for liver tissue engineering," *J Biomed Mater Res A*, **102**(11), pp. 4169-81.
- [67] Yazdimamaghani, M., Razavi, M., Mozafari, M., Vashae, D., Kotturi, H., and Tayebi, L., 2015, "Biom mineralization and biocompatibility studies of bone conductive scaffolds containing poly(3,4-ethylenedioxythiophene):Poly(4-styrene sulfonate) (pedot:Pss)," *Journal of materials science. Materials in medicine*, **26**(12), pp. 274.
- [68] Feng, Z.Q., Chu, X., Huang, N.P., Wang, T., Wang, Y., Shi, X., Ding, Y., and Gu, Z.Z., 2009, "The effect of nanofibrous galactosylated chitosan scaffolds on the formation of rat primary hepatocyte aggregates and the maintenance of liver function," *Biomaterials*, **30**(14), pp. 2753-63.
- [69] Kim, J., Magno, M.H., Waters, H., Doll, B.A., McBride, S., Alvarez, P., Darr, A., Vasanji, A., Kohn, J., and Hollinger, J.O., 2012, "Bone regeneration in a rabbit critical-sized calvarial model using tyrosine-derived polycarbonate scaffolds," *Tissue engineering. Part A*, **18**(11-12), pp. 1132-9.
- [70] Shanjani, Y., Pan, C.C., Elomaa, L., and Yang, Y., 2015, "A novel bioprinting method and system for forming hybrid tissue engineering constructs," *Biofabrication*, **7**(4), pp. 045008.